Nat. Hazards Earth Syst. Sci. Discuss., 2, 1259–1331, 2014
www.nat-hazards-earth-syst-sci-discuss.net/2/1259/2014/
doi:10.5194/nhessd-2-1259-2014

Natural Hazards and Earth System Sciences
Discussions

Landslides triggered by the 12 January 2010 Mw 7.0 Port-au-Prince, Haiti, earthquake: visual interpretation, inventory compiling and spatial distribution statistical analysis

C. Xu[1,2], J. B. H. Shyu[2], and X.-W. Xu[1]

[1]Key Laboratory of Active Tectonics and Volcano, Institute of Geology, China Earthquake Administration, Beijing 100029, China
[2]Department of Geosciences, National Taiwan University, Taipei, Taiwan

Received: 17 January 2014 – Accepted: 30 January 2014 – Published: 10 February 2014

Correspondence to: J. B. H. Shyu (jbhs@ntu.edu.tw) and C. Xu (xc11111111@126.com)

Published by Copernicus Publications on behalf of the European Geosciences Union.

Abstract

The 12 January 2010 Port-au-Prince, Haiti, earthquake (Mw 7.0) triggered tens of thousands of landslides. The purpose of this study is to investigate the correlations of the occurrence of landslides and their erosion thicknesses with topographic factors, seismic parameters, and their distance from roads. A total of 30 828 landslides triggered by the earthquake covered a total area of 15.736 km^2, distributed in an area more than 3000 km^2, and the volume of landslide accumulation materials is estimated to be about 29 700 000 m^3. These landslides are of various types, mostly belonging to shallow disrupted landslides and rock falls, but also include coherent deep-seated landslides and rock slides. These landslides were delineated using pre- and post-earthquake high-resolutions satellite images. Spatial distribution maps and contour maps of landslide number density, landslide area percentage, and landslide erosion thickness were constructed in order to analyze the spatial distribution patterns of co-seismic landslides. Statistics of size distribution and morphometric parameters of co-seismic landslides were carried out and were compared with other earthquake events in the world. Four proxies of co-seismic landslide abundance, including landslides centroid number density (LCND), landslide top number density (LTND), landslide area percentage (LAP), and landslide erosion thickness (LET) were used to correlate co-seismic landslides with various landslide controlling parameters. These controlling parameters include elevation, slope angle, slope aspect, slope curvature, topographic position, distance from drainages, lithology, distance from the epicenter, distance from the Enriquillo–Plantain Garden fault, distance along the fault, and peak ground acceleration (PGA). A comparison of these impact parameters on co-seismic landslides shows that slope angle is the strongest impact parameter on co-seismic landslide occurrence. Our co-seismic landslide inventory is much more detailed than other inventories in several previous publications. Therefore, we carried out comparisons of inventories of landslides triggered by the Haiti earthquake with other published results and proposed possible reasons of any differences. We suggest that the empirical functions between earthquake

magnitude and co-seismic landslides need to update on the basis of the abundant and more complete co-seismic landslide inventories recently available.

1 Introduction

At 16:53 LT on 12 January 2010, a catastrophic earthquake with Mw 7.0 struck the Port-au-Prince region of Haiti (Calais et al., 2010). The epicenter was located at latitude 18°27′25″ N, longitude 72°31′59″ W, approximately 15 km southwest of Port-au-Prince and close to the surface trace of the Enriquillo–Plantain Garden fault, with a focal depth of 13 km according to the National Earthquake Information Center, US Geological Survey (NEIC, 2010). The earthquake caused widespread damage in and west of the capital city of Port-au-Prince, and killed more than 230 000 people (Bilham, 2010; Bellerive, 2010; Calais et al., 2010; Hough et al., 2010; Koehler and Mann, 2011). The earthquake also triggered extensive landslides, some of which caused damages such as blocked roads, dammed rivers and streams, and threatened infrastructures in many parts of Haiti (Eberhard et al., 2010; Jibson and Harp, 2011; Stumpf and Kerle, 2011; Xu et al., 2012).

Co-seismic landslide inventory compiling is essential for associated co-seismic landslides studies, and spatial distribution statistical analysis of those landslides is important in understanding which areas are most susceptible to landsliding in future earthquakes. Early studies of landslide inventory compiling and simple spatial distribution analysis have been summarized by Keefer (1984, 1999, 2002) and Rodríguez et al. (1999). In recent years, more and more studies of co-seismic landslides related to individual earthquake events have emerged. Table 1 listed the inventories of co-seismic landslides triggered by 21 main earthquakes worldwide in recent years based on field investigations and/or GIS and remote sensing technologies.

The 2010 Haiti earthquake provides us a good opportunity to compile a detailed co-seismic landslide inventory and to study the spatial distributions and effects of landslides triggered by a transpressional-fault related earthquake in a subduction zone. The

main purpose of this study is to characterize the spatial distribution of landslides triggered by the Haiti earthquake by correlating four proxies of co-seismic landslide abundance, including landslide centroid number density (LCND), landslide top number density (LPND), landslide area percentage (LAP), and landslide erosion thickness (LET), to various impact factors that control the occurrence of co-seismic landslides. These factors include elevation, slope angle, slope aspect, slope curvature, topographic position, distance from drainages, lithology, distance from the epicenter, distance from the Enriquillo–Plantain Garden fault, distance along the fault, and peak ground acceleration (PGA). In addition, size distributions and morphometric parameters of co-seismic landslides were analyzed and compared with co-seismic landslides triggered by other events in the world. We also compared the controls of seven impact parameters on co-seismic landslides, and the results show that slope angle has the strongest control on co-seismic landslide occurrence. Finally, we analyzed the differences between our new inventory of landslides triggered by the Haiti earthquake and other inventories.

2 Tectonic setting

The Haiti earthquake occurred in a complex deformation zone that separates the North America plate and the Caribbean plate (Mann et al., 1984; Frankel et al., 2010; DesRoches et al., 2011). Global positioning system (GPS) studies show this plate boundary zone is dominated by left-lateral strike slip motion and compression with a rate of about 20 mm yr^{-1}, with the Caribbean plate moving east-northeastward with respect to the North America plate (Fig. 1; Dixon et al., 1998; DeMets et al., 2000; Manaker et al., 2008; Calais et al., 2010; Prentice et al., 2010). This results in the oblique convergence between the two plates (Dixon et al., 1998; Mann et al., 2002; Calais et al., 2010). There are three main fault systems in this area, including the North Hispaniola fault zone (NHFZ), Septentrional fault zone (SFZ), and the Enriquillo–Plantain Garden fault zone (EPGFZ) (Fig. 1; Mann et al., 1984; Calais and de Lépinay, 1991; Calais et al., 1992, 1998, 2010; Frankel et al., 2010). In addition, there are also thrust

faults within the island that accommodate the compressional component of the motion (Frankel et al., 2010).

The epicenter of the earthquake was located near the Enriquillo–Plantain Garden Fault (Fig. 1), which accommodates part of the oblique convergence between the North America and the Caribbean plates (Wdowinski and Hong, 2010). The fault is a major structural feature that cuts through the center of the southern peninsula of Haiti, and an emergent oceanic plateau complex of Late Cretaceous age crops out along the fault (Koehler and Mann, 2011). In this study, the Enriquillo–Plantain Garden fault was mapped on the basis of its geomorphic expression in the study area using satellite imagery, SRTM and ASTER GDEM. Along most of its length, the fault is topographically well expressed as a strong, linear, N85° E-trending feature in the landscape (Eberhard et al., 2010; Prentice et al., 2010). The fault system is characterized by several prominent stopovers that result in pull-apart basins at extensional left steps and high topographic push-ups at compressional right steps, consistent with active left-lateral strike-slip motion (Mann et al., 1995; Prentice et al., 2010). Prominent tectonic geomorphic features of the fault include long, linear river valleys, restraining bend push-up blocks, extensional basins along releasing bends, captured drainages, and north- and south-facing mountain escarpments (Koehler and Mann, 2011). Related structural features include northwest-trending anticlines, synclines, and thrust faults (Mann et al., 1984, 1995; Koehler and Mann, 2011).

The earthquake had a complex mechanism that includes both thrust and left-lateral strike-slip movement (Jibson and Harp, 2011). This focal mechanism is consistent with oblique left-lateral strike-slip motion along a 252°-striking nodal plane or oblique thrusting along a northwest-striking plane. Preliminary finite fault model results indicate a maximum slip of about 4.5 m (about 1.8 m in average) with little deformation at the surface (NEIC, 2010). Many crustal earthquakes with Mw 7.0 or greater are accompanied by surface ruptures that can be traced for tens of kilometers. Thus the earthquake was initially thought to have occurred along the Enriquillo–Plantain Garden fault with surface ruptures. However, no surface rupture was identified after extensive

investigations (Eberhard et al., 2010; Hayes et al., 2010; Prentice et al., 2010; Koehler and Mann, 2011). Later, several studies showed that the earthquake instead occurred on a previously unmapped north-dipping Léogâne fault subparallel to the Enriquillo–Plantain Garden fault (Calais et al., 2010; Hayes et al., 2010; Prentice et al., 2010; Hashimoto et al., 2011; de Lépinay et al., 2011). In fact, earthquakes of similar magnitude may also occur without accompanying surface ruptures. For example, the 18 October 1989 Loma Prieta, California, earthquake (Mw 6.9) was a similar-size, shallow, oblique-slip earthquake that occurred close to a major strike-slip fault but was not accompanied by surface ruptures (Prentice and Schwartz, 1991; Árnadóttir and Segall, 1994; Prentice et al., 2010).

Based on historical earthquake records of the area, this event was one of the most disastrous Mw 7.0 earthquakes, joining the 15 September 1751, 21 November 1751, and 3 June 1770 events that also caused widespread destruction in Port-au-Prince and the surrounding regions (Scherer, 1912; Ali et al., 2008; Prentice et al., 2010). Although the locations of these historical events are poorly known, they are thought to have occurred on the Enriquillo–Plantain Garden fault and/or the Muertos fault (MF) system (Fig. 1). This, however, has not been confirmed in the field (Koehler and Mann, 2011; Calais et al., 2010; Scherer, 1912; Prentice et al., 2010; Manaker et al., 2008). The aftershock sequence of the 2010 event extended predominantly west of the epicenter for about 60 km and includes 59 earthquakes with magnitude 4.5 or greater. The aftershocks distributed across an area about 30 km wide. The two largest aftershocks, with M 6.0 and M 5.9, occurred seven minutes after the main shock and on 20 January, eight days after the main shock. The aftershocks show predominantly strike-slip focal mechanisms, but several events with thrust mechanism also occurred (Koehler and Mann, 2011).

3 Bedrock geology of the study area

We obtained the bedrock information from the geological map of "Carte Geologique D'Haiti, Feuille Sud-Est: Port-au-Prince", with a scale of 1 : 250 000 (Lambert et al., 1987). According to the map, there are 14 classes of bedrock lithologies (Fig. 2), which are:

3.1 Sedimentary rocks (Quaternary)

1: Qa: Alluvium, fluvial cones, gravels, mangrove-related sediments or deposits.

2: Qc: limestone, marine terraces.

3.2 Sedimentary rocks (Tertiary)

3: P: Pliocene. Marls and sandstones, old cones, marls and sands of the Central Plateau and Gros Morne basin.

4: Ms: Upper Miocene. Marl, marl and sandstone of the Central Plateau and Gros Morne basin.

5: Mi: Lower Miocene. Sand clay-clay flysch sandstone of the Central Plateau; calcareous sandstone of Gros Morne basin, limestone of Chaînon mountain of Paincroix and Peninsula South Island.

6: O: Oligocene. Limestone and marl of South Island and Matheux mountain; clays and sandstones of Gros Morne basin; coarse limestone and conglomerates (on the edge of Canal of Tortue).

7: Es: Upper Eocene. Pelagic limestones of the Selle Massif.

8: Ems: Upper Mid-Eocene. Pelagic biomicrites of the South Island and southern slopes of the Nord Massif; limestone of the platform of the Nord Massif.

9: Ep: Upper Paleocene, Lower to Middle Eocene. Volcanogenic conglomerates and sandstones of the Selle Massif; marl, sandstone and limestone marl of the Black Mountains; limestone on the platform and pelagic limestones.

3.3 Sedimentary rocks (Cretaceous and Tertiary)

10: Pi: Maastrichtian to Danian. Marl and limestones of the Selle Massif; clay and volcanic detrital rocks of the Hotte Massif; also pelagic limestones of the South Island.

3.4 Sedimentary rocks (Cretaceous)

11: Cs: Cretaceous (Senonian). Pelagic limestones of the South Island and the Massif of Newfoundland, and other limestones of the same age.

12: Cc: Lower to Middle Cretaceous. Calcarenites and red marls of the South Island.

3.5 Igneous rocks (Cretaceous)

13: Ca: Series of blocks of Jacmel road.

14: Cb: Complex tholeiitic and sedimentary rocks of the South Island and other massive flows with or without sedimentary intercalations.

4 Landslides triggered by the earthquake

4.1 Visual interpretation of landslides triggered by the earthquake

A detailed and comprehensive co-seismic landslide inventory is important for subsequent landslides spatial distribution analysis and hazard assessment, as well as other studies of earthquake-triggered landslides (Keefer, 2002; Harp et al., 2011; Guzzetti et al., 2012; Xu, 2014; Stumpf and Kerle, 2011). After the Haiti earthquake, Jibson and Harp (2011) carried out field investigations of some of the co-seismic landslides. However, for the very large amount of landslides triggered by the Haiti earthquake, to prepare a landslide inventory only based on field investigations is unrealistic. On the other hand, the availability of many high-resolution satellite images on the Google Earth platform allowed researchers to conduct a more detailed visual interpretation

of earthquake-triggered landslides. This allowed us to construct a detailed inventory of landslides triggered by the 2010 Haiti earthquake. In this study, we followed several principles for the landslide visual interpretation based on high-resolution satellite images: (i) all landslides that can be recognized in the images should be mapped; (ii) both landslide boundaries and the positions of landslide source area should be mapped; and (iii) complex landslides should be divided into individual ones.

In addition, it is necessary to distinguish co-seismic landslides from pre-earthquake landslides and post-earthquake landslides triggered by rainfall or other events. We have used the following criteria during the landslide visual interpretation processes: (i) if a landslide did not exist on the pre-earthquake image but exists on post-earthquake images, it is considered a co-seismic landslide. (ii) If there are more than one remote sensing images taken after the earthquake at different times, a landslide exists on later images but is absent on older images is considered a post-earthquake landslide triggered by rainfall or other events, rather than a co-seismic landslide. (iii) If a landslide exists on both pre- and post-earthquake images and shows the same morphology and texture, it is considered a pre-earthquake landslide not triggered by the earthquake. More detailed criteria of distinguishing pre-earthquake, co-seismic, and post-earthquake landslides were listed in Xu (2014).

Here we show several examples of landslides that we do not consider as co-seismic landslides triggered by the Haiti earthquake. Figure 3 are two sets of pre- and post-earthquake satellite images that show several pre-earthquake landslides were not affected by the earthquake. Figure 3a and b show a landslide that existed in the image taken on 10 May 2008 (brightness part) and showed the same shape on the image taken on 13 January 2010. Thus the landslide is not considered as a co-seismic landslide. Similarly, Fig. 3c and d show pre- and post-earthquake images of several landslides. There is no clear shape change of the landslide in the images, thus we also consider these landslides as pre-earthquake landslides and excluded them from the landslide inventory related to the Haiti earthquake. In Fig. 4, on the other hand, we show a landslide triggered by post-earthquake rainfall or other events rather than the

main shock. The landslide was absent in the image of Fig. 4a, taken on 18 August 2010, but can be clearly observed in the image of Fig. 4b, taken on 9 November 2010. This shows the landslide was not triggered by the earthquake but most probably triggered by a rainfall event between 18 August and 9 November 2010.

Figure 5 shows two sets of images in three acquisition times. No landslide was present in the image of Fig. 5a, taken on 4 February 2009 (pre-earthquake). After the earthquake occurred, a landslide appeared to be triggered by the earthquake and showed up in the image (Fig. 5b) taken on 13 January 2010. Later, the landslide was enlarged as shown in Fig. 5c most probably by subsequent rainfall events. Figure 5d–f shows another similar case of a landslide most likely triggered by the Haiti earthquake and enlarged by subsequent rainfall events. Therefore, when delineating co-seismic landslides, we need to observe the initial images as soon after the earthquake occurred as possible (e.g., Fig. 5b and e).

4.2 Landslide classification

Field investigations show most of the landslides triggered by the Haiti earthquake were mainly of disrupted rock falls and rock slides in the limestone and weathered basalt that are the dominant bedrocks in the region surrounding the Enriquillo–Plantain Garden fault (Jibson and Harp, 2011). Many of the landslides blocked stream drainages and impounded lakes. Some of the larger landslide dams had already been breached, and the streams were flowing through them in a stable state (Jibson and Harp, 2011). Landslide densities were the greatest in deeply weathered, sheared, fractured, and altered limestone, but weather basalt slopes produced much fewer landslides (Jibson and Harp, 2011). In this study, we classified the landslides triggered by the Haiti earthquake into four classes based on the correlations of published field investigation results (Jibson and Harp, 2011) and high-resolution satellite images. These classes include coherent deep-seated landslides, shallow disrupted landslides, rock falls, and rock slides. The definitions of the four terminologies are summarized in Keefer (1984, 2002).

4.2.1 (i) Coherent deep-seated landslides

Figure 6 shows a group of co-seismic coherent deep-seated landslides triggered by the Haiti earthquake. Figure 6a shows two such landslides composed by sandstone and limestone and about 100 m apart. The areas of the two landslides are about 12 500 m^2 and 20 000 m^2. The left one is 160 m long and 100 m wide, and the right one is 220 m long and 100 m wide in its widest part. The right one dammed the stream and formed a small lake. Figure 6b show a coherent landslide composed by sandstone and limestone. The area of the landslide is about 8500 m^2. The highest length and width of the landslide body are about 130 m and 90 m. The elevations of the landslide crown and the shear opening materials are about 370 m and 350 m, respectively. This indicates the landslide occurred on a relatively gentle slope. Figure 6c shows a deep-seated landslide composed by sandstone and limestone (unit Mi in the bedrock geology) and with an area of about 13 000 m^2. The highest length and width of the landslide are about 180 m and 100 m. This landslide also blocked a stream and formed a small dammed lake. Figure 6d shows another co-seismic deep-seated landslide about 20 000 m^2 that occurred in limestone bedrocks. The highest length and width of the landslide are about 210 m and 120 m. All of the coherent deep-seated landslides in Fig. 6 showed a slight to moderate amount of internal disruption and short movement distances of the landslide bodies. Such landslides are unusual compared with the other three landslide types.

4.2.2 (ii) Shallow disrupted landslides

Shallow disrupted landslides are the major type of co-seismic landslides in earthquakes worldwide (Keefer, 2002). Such landslides are often small, less than 10 000 m^3, and show coalescing landslide complexes. Figure 7 shows two sets of pre- and post-earthquake images with dense co-seismic shallow disrupted landslides.

4.2.3 (iii) Rock falls

The movement types of rock falls include bouncing, rolling, and free fall. They are often related with joints and fractures oblique to the foliation and with high internal disruption. Figure 8 shows a group of rock falls triggered by the Haiti earthquake. Figure 8a shows a rock fall of about 3500 m^2 composed by limestone. Its estimated volume is about 7000 m^3. Figure 8b shows several rock falls that occurred on a steep coastal cliff composed by limestone. Total area of the rock falls in the white rectangle (Fig. 8b) is about 35 000 m^2, with a total volume of about 100 000 m^3. The highest elevation of landslide materials is about 140 m and part of these materials moved into the sea. Figure 8c shows a large rock fall and several smaller rock falls that occurred on a south-facing slope, with an approximate area of 26 000 m^2 and volume of 80 000 m^3. The bedrock geology of the area is limestone (unit Ems). Figure 8d mainly shows two rock falls (i and ii) and one deep-seated landslide (iii) that occurred on bedrocks of sandstone and limestone (unit Mi). The (i) and (ii) rock falls were about 5300 m^2 and 2400 m^2 in area, with estimated volumes of about 10 000 m^3 and 4000 m^3, respectively. The rock fall (ii) blocked a stream and formed a small dammed lake. Between the two rock falls, a deep-seated landslide also occurred. It is about 4400 m^2 and with an estimated volume of 10 000 m^3. It is noteworthy that the rock fall (ii) also likely occurred at the front of the deep-seated landslide body.

4.2.4 (iv) Rock slides

Unlike rock falls, rock slides often occur on dip slopes with continuous slipping surface and are often with high internal disruption. Figure 9 shows several rock slides triggered by the Haiti earthquake. Figure 9a shows a rock slide with an area of about 44 000 m^2 and a volume about 200 000 m^3. The landslide materials are composed by sandstone and limestone, and moved from the top elevation of 400 m to 240 m. The longest horizontal runout distance is about 300 m and the largest width is nearly 150 m. Figure 9b shows a rock slide with an area of about 24 000 m^2 and a volume about 100 000 m^3.

The landslide materials are also composed by sandstone and limestone. Figure 9c shows a relatively small rock slide of about 2500 m^2 in area and 5000 m^3 in volume. The landslide also occurred in the unit Mi containing sandstone and limestone. In Fig. 9d, a rock slide of about 3700 m^2 in area and 8000 m^3 in volume dammed a stream. The landslide materials are composed by limestone in the unit Ems.

4.3 Landslide inventory

Within days after the Haiti earthquake, a large number of pre-and post-earthquake satellite images were available on Google Earth (last accessed September 2011) and facilitated the preparing of detailed inventories of earthquake-triggered landslides (Jibson and Harp, 2011; Koehler and Mann, 2011). Although there have been a few publications (Jibson and Harp, 2011; Harp et al., 2013; Gorum et al., 2013) about landslides triggered by the Haiti earthquake, due to the more and more available high-resolution satellite images on the Google Earth platform, the initial inventories appear not very complete. Therefore, we decided to carry out a thorough visual interpretation of co-seismic landslides and to prepare a more detailed landslide inventory. We have utilized available satellite images with sufficiently high resolution to identify and map all but the smallest landslides triggered by the Haiti earthquake. An individual landslide was delineated as a solid polygon, and the location of landslide crown was also plotted as a point. In the end, 30 828 individual landslides triggered by the earthquake were detected. In addition, centroids of these landslide polygons were also extracted for the subsequent landslide spatial distribution analysis. The smallest landslide triggered by the earthquake detected in this study only had a surface area of about 1 m^2 due to the very high resolution and quality of satellite images on Google Earth.

Our results show that the Haiti earthquake triggered more than 30 000 landslides in an asymmetrical distribution pattern (Fig. 10). The landslides distributed in an area about 3000 km^2, with a width of about 90 km in the east–west direction and centered at the epicenter, and over the entire north–south extent of the onland part of the peninsula (Fig. 10). The landslides covered a total area of about 15.736 km^2. The land-

slide area percentage (LAP), which is expressed as a percentage of the area affected by landslide activity, was LAP = (15.736 km^2/3192.85 km^2) × 100 % = 0.493 %, and the landslide number density (LND), which is calculated as the number of landslides per square kilometer, was LND = 30 828 landslides/3192.85 km^2 = 9.655 landslides km^{-2}. In addition, in order to carry out statistics of co-seismic landslide erosion (landslide volume), we used a simple scaling relationship to convert individual landslide area to individual landslide volume:

$$V_i = \alpha \times A_i^{\gamma} \quad (1)$$

where V_i is the volume of a landslide (the i landslide) and A_i is the area of the landslide. The two scaling parameters α and γ are constants varying with different landslide types and cases. Since we do not have information of actual volumes of the landslides triggered by the Haiti earthquake to invert the two constants, we assigned the two constants as $\alpha = 0.146$ and $\gamma = 1332$, which are derived from various types of landslides based on a previous study (Larsen et al., 2010). The volumes of each individual landslide can therefore be derived respectively based on the area and Eq. (1). The total volume of all landslides was calculated as about 29 700 000 m^3. Thus the landslide erosion thickness (LET) of the study area is 29 700 000 m^3/3192.85 km^2 = 9.3 mm. Keefer (1994) proposed a regressed relation between the seismic moment and the volume of landslides related to an individual earthquake event as $V = Mo/10^{18.9(\pm 0.13)}$, where Mo is measured in dyn·cm and V is in m^3. The relation was applied to the Irpinia region, Italy, and a quantitative measure of the long-term hazard from earthquake-triggered landslides was provided (Parise, 2000). The seismic moment of the Haiti earthquake is 4.39×10^{26} dyn·cm (http://www.globalcmt.org/CMTsearch.html). Therefore, the total landslide volume can be calculated as about 55 300 000 m^3 (41 000 000–74 600 000 m^3). This is higher than our calculation, but within the same order of magnitude.

As shown in Fig. 10, there are two landslide high density areas (areas I and II). Both areas are ellipse-shaped. The area II is located east of the epicenter, with east–west

trending long axis. The epicenter is located approximately at the western end of the long axis. The area I is located about 20 km southwest of the epicenter and direction of its long axis is northwest–southeast trending.

In order to prepare maps of LND, LAP, and LET of the study area, we constructed 1 km × 1 km grid cells throughout the area (Fig. 10). All vertical and horizontal lines are in integer kilometer coordinates (the map projection is WGS_1984_Lambert_Conformal_Conic, with the Central_Meridian: −72.5, Standard_Parallel_1: 18.0, Standard_Parallel_2: 18.5, and Latitude_Of_Origin: 18.0). The results show the highest LND and LAP values are in grid "a" in Fig. 10, with 349 landslides km^{-2} and 24.4 %, respectively. The pre- and post-earthquake images of grid "a" are shown in Fig. 11a and b. The LET of grid "a" is 489 mm. The largest LET value, which is about 680 mm, is found in grid "b" in Fig. 10. The pre- and post-earthquake images of this grid are shown in Fig. 11c and d. Although grid "b" has the largest LET value, the LND and LAP values of this grid are not very high, only 136 landslides km^{-2} and 15.6 %, respectively. This is due to a deep-seated landslide and a large shallow disrupted landslide that are the major landslides in this grid (Fig. 11c and d). In addition, we prepared distribution maps and contour maps of LND, LAP, and LET, respectively. Figure 12 shows the distribution map and contour map of LAP. The contour interval in Fig. 12b is 1 %.

4.4 Landslide size and morphometric parameters

The co-seismic landslide cumulative number–area and number–volume relationships are shown in Fig. 13. Similar to landslides triggered by other earthquake events (Xu et al., 2014; Dai et al., 2011), the two curves bend towards horizontal at small landslide areas. This indicates it is very difficult to obtain a complete sample for small landslides even though we have used high-resolutions satellite images to map co-seismic landslides. There are several reasons for this, including: (i) small-scale landslides may be covered by large landslides; (ii) several coalescing small-scale landslides may be mapped as a large landslide; (iii) human generated omission (false negative) errors

that result in overlooking small-scale landslides, due to the large number and distribution area and the high density of landslides triggered by the Haiti earthquake. However, in Fig. 13a, there is an obvious inflection point of the curve at landslide area of about 100 m^2. Therefore, the inventory of landslides of area larger than 100 m^2 should be quite complete and comprehensive. The colored background of Fig. 13a shows the density of landslide points, and most of the co-seismic landslides fall in the area between 10 and 1000 m^2. In fact, 26 661 landslides, which are 86.5 % of the total number, are in this area range. Figure 13b shows a similar trend as Fig. 13a. A total of 23 642 landslides, or 76.7 % of the total number, fall in the volume range between 10 m^3 and 1000 m^3.

Simple morphometric parameters of the co-seismic landslides, including length, width, height, aspect ratio, and angle of reach, were analyzed. Length (the horizontal distance from the crown of a landslide to its tip) was computed along the direction of landslide movement. Width was measured as the average width, calculated as the area divided by length. Height was measured as the elevation difference between the crown of a landslide and its tip. The shape of a landslide can be described by its aspect (length/width) ratio (Parise and Jibson, 2000; Xu and Xu, 2014). Generally, a high aspect ratio is typical of flow-type landslides or disrupted slides, whereas a low value mostly corresponds to a rotational landslide (Parise and Jibson, 2000). Previous studies show that the average aspect ratios associated with landslides triggered by the 1994 Northridge, California, M 6.7 earthquake (Parise and Jibson, 2000) and the 2010 Yushu, China, Mw 6.9 earthquake (Xu and Xu, 2014) were about 4.15 and 2.6, respectively. Figure 14 shows the correlations between landslide aspect ratio and landslide number. The ratios of most landslides (29 116 landslides, or 94.4 % of the total number) are less than 8. The statistical result shows that aspect ratios of the landslides triggered by the Haiti earthquake range from 1.37 to 53.4, and the average aspect ratio is 3.76. This result shows that the average landslide aspect ratio related to the Haiti earthquake is similar to that of the Yushu earthquake-triggered landslides, and that both of them are greater than the average aspect ratio related to the Northridge earthquake-

triggered landslides. This is probably because the magnitudes of the Haiti and Yushu events are higher than that of the Northridge event. The larger magnitude resulted in more strong ground motion and peak ground acceleration. For the Yushu event, there were almost no coherent landslides due to the special geology of the area (Xu and Xu, 2014), but there were more coherent landslides triggered by the Haiti earthquake (Fig. 6) that have lower aspect ratios. Therefore, the average aspect ratio of landslides triggered by the Haiti earthquake is slightly lower than that of landslides triggered by the Yushu earthquake.

Height (H)/length (L) ratio is another landslide morphometric parameter. Qi et al. (2011) carried out a statistic analysis of height/length ratios of 66 long runout rock avalanches and obtained a relationship that is $H = 0.2638L + 212.4$. In this study, a total of 453 Haiti earthquake-triggered landslides of volume larger than 10 000 m^3 were used to construct a similar relationship (Fig. 15). We mandatorily set the intercept to the origin since both the horizontal runout length and height should be zero as landslides become small enough. Based on the 453 landslides, we obtained a relationship, $H = 0.595L$, with $R^2 = 0.6972$. The coefficient is 0.595, which is much higher than the 0.2638 derived from 66 long runout rock avalanches triggered by the 2008 Wenchuan earthquake (Qi et al., 2011). This is because the landslides of the Wenchuan earthquake were larger rock avalanches and they had long runout distances due to the strong ground motion, whereas the 453 landslides triggered by the Haiti earthquake contain various landslide types and experienced relatively gentle ground motion comparing with the Wenchuan event, thus have relatively short runout distances.

Landslide angle of reach is calculated as the arctangent of height/length value. Figure 16 and Table 2 show the distribution of angle of reach of three different groups of landslides, including 19 889 landslides of area larger than 100 m^2, 3564 landslides of area larger than 1000 m^2, and 103 landslides of area larger than 10 000 m^2. Angle of reach distributions with landslide number and landslide number percentage were constructed based on the three groups of landslides. The results show landslides of angle of reach between 5° and 15° are the most with area larger than 100 m^2. For landslides

of area larger than 1000 m^2, the main range of angle of reach is between 15° and 30°. The result of landslides of area larger than 10 000 m^2 shows that the most frequent range of angle of reach is 25–40°. There is thus a tendency that the angle of reach of larger landslides is generally higher than that for smaller ones. This perhaps because the coherent deep-seated landslides of large areas mostly have higher angle of reach due to their smaller horizontal runout distance, whereas shallow-disrupted landslides of small areas have lower angle of reach due to their larger horizontal runout distance.

5 Co-seismic landslides controlling parameters analysis

The occurrence of landslides in an earthquake can be related to topographic, geologic, and earthquake parameters. For the Haiti earthquake-triggered landslides, the correlations of the landslides with controlling parameters were performed using four indexes of landslide abundance, including landslide centroid number density (LCND), landslide top number density (LTND), landslide area percentage (LAP), and landslide erosion thickness (LET). A total of 11 parameters were selected, including six topographic parameters (elevation, slope angle, slope aspect, slope curvature, topographic position, and distance from drainages), one geological parameter (lithology), and four earthquake parameters (distance from the epicenter, distance from the main fault-EPGF, distance along the EPGF, and PGA).

5.1 Topographic parameters

The available DEM of the study area include the SRTM DEM and ASTER GDEM in about 90 m and 30 m resolutions, respectively. However, since only 4029 co-seismic landslides had area larger than 900 m^2 (the area of one grid of ASTER GDEM), we resampled the ASTER GDEM into a new pseudo high-resolution DEM in 5 m resolution. Although the resampling process will not increase any more detailed terrain information, it will not reduce or change the topographical information in a regional scale either.

Then, landslide polygon map of vector format can be converted into a grid cell format in 5 m resolution. The errors can be greatly reduced comparing with converting into landslide raster map in 30 m resolution. Subsequently, thematic maps of slope angle, slope aspect, slope curvature, and topographic position were derived from the 5 m resolution DEM based on the GIS platform.

The elevations of the study area are from 0 m to 2275.88 m and with an average elevation of 522.29 m. Thus we divided the study area into ten classes, including 1: < 200 m, 2: 200–400 m, 3: 400–600 m, 4: 600–800 m, 5: 800–1000 m, 6: 1000–1200 m, 7: 1200–1400 m, 8: 1400–1600 m, 9: 1600–1800 m, 10: > 1800 m. Correlations of elevation with the areas of classes, LCND, LPND, LAP, and LET are shown in Fig. 17. It can be observed that the area of classes decreases with increasing elevation, and most of the study area is at low altitude. There is no evident correspondence between co-seismic landslides and elevation. Landslide abundances of the classes 2–6 (elevations of 200–1200 m) show the largest values. Different tendencies of LCND/LPND curves and LAP/LET curves indicate uneven distribution characteristic of similar-scale landslides in different elevation classes. The class 4 (600–800 m) appears to register larger-scale landslides due to its high LAP value and relatively low LCND and LPND values. The maximum values of LCND and LPND are 13.61 and 13.53 landslides km^{-2}, respectively, and both of them appear at class 2 (200–400 m). The largest LAP and LET values, both occur at class 4 (600–800 m), are 0.712 % and 14.52 mm. The LTND curve appears slightly towards the direction of higher elevations since top point elevation of a landslide is higher than its centroid point.

The slope angle range of the study area is 0–75.83° and was classified in intervals of 5°. The average slope angle of the study area is 15.24°, and most slopes of the study area are relatively gentle. According to the 5° interval of slope angle, the study area was divided into 11 classes. Relationships of slope angle with areas of classes and landslide abundances were shown in Fig. 18. Slope angles of most of the study area (about 2902 km^2, 90.9 % of the study area) are less than 30°. When the slope angle is higher than 10°, the steeper the slopes are, the smaller area they cover. The

four landslide abundance proxies (LCND, LPND, LAP, and LET) show similar correlations with slope angle (Fig. 19). This indicates various scales of co-seismic landslides distributed in all slope angle classes. Except for classes 10 and 11 (> 45°) that only cover small areas (13.05 km^2 and 8.38 km^2, or 0.409 % and 0.263 % of the study area, respectively), all of the four landslide abundance proxies show a rising tendency with increasing slope angles. Such results suggest a strong control of slope angle on co-seismic landslide occurrence, similar to other earthquake events worldwide (Dai et al., 2011; Gorum et al., 2011, 2013; Xu et al., 2014). All of the maximum LCND, LPND, and LAP values occurred at class 10 (45–50°), and their values are 50.12 and 50.73 landslides km^{-2}, and 3.498 %. The maximum LET value of 78.93 mm, however, occurred at class 9 (40–45°).

Slope aspect may also influence co-seismic landslide occurrence because different slope aspect may receive different effect related to the slipping direction of the seismogenic fault and the propagating direction of seismic waves. We divided slope aspect of the study area into nine classes, including flat, north, northeast, east, southeast, south, southwest, west, and northwest. The statistical result (Fig. 19) shows the relationship between co-seismic landslide abundance and slope aspect. As shown in Fig. 19, east-facing slopes (class 4) have the most landslides. This may correspond with the moving direction of the southern block of the Enriquillo–Plantain Garden fault, since most of the study area is located south of the fault. This indicates that the favorite slope orientation for landslide occurrence is corresponding with the direction of crustal movement. In addition, the east direction is also consistent with the principal stress direction of the earthquake struck area long before the earthquake. Such phenomena have also been observed in other earthquake events, including the 2008 Wenchuan, China, earthquake (Xu et al., 2014), the 2010 Yushu, China, earthquake (Xu et al., 2013a), and the 2013 Lushan, China, event (Chen et al., 2013; Xu and Xiao, 2013). The curves of LCND and LTND, LAP, and LND show different trends in Fig. 19. This indicates different scaled landslides concentrate in different classes of slope aspect. For example, many small-scaled landslides appeared to occur on south-facing slopes due

to the LAP value of the class is relatively small. All of the maximum values of LCND, LTND, LAP, and LET appear at class 4 (east-facing slopes) and the values are 15.09 landslides km^{-2}, 15.03 landslides km^{-2}, 0.709 %, and 13.79 mm, respectively. In general, the curves of LCND and LTND are coincident since the slope aspect of the top and centroid points of a landslide are almost the same.

Slope curvature represents the shapes of the slopes. Positive values mean convex slopes, negative values indicate concave slopes, and values close to zero represent flat-surface slopes. We divided slope curvature of the study area into 12 classes. The correlations between slope curvature values, areas of the classes, and LCND, LTND, LAP, and LET values are shown in Fig. 20a. The area of classes 6 and 7 (slope curvature values of −0.1 to 0.1) are the largest, and this means most of the study area are covered by relatively flat-surface slopes. In general, when slope curvature gets closer to zero, the values of landslide abundance proxies (LCND, LTND, LAP, and LET) become smaller. This suggests flat-surface slopes are less prone to co-seismic landslides than convex or concave slopes. The four landslide proxies show a similar trend, which indicates that the scales of co-seismic landslides were not affected by slope curvature values. Unlike most other topographic parameters, the LCND and LTND values show clear differences. For concave slopes, LCND values are always higher than LTND values, whereas it is the opposite for convex slopes. This indicates landslide top points are more likely to locate at convex slopes than concave slopes. This is probably because top points of landslides usually correspond to convex slopes such as ridges, isolated peaks, and convex rocks, etc., whereas centroids of landslides corresponds to slope bodies that are not convex slopes. All of the maximum values of the four indexes occurred at class 1 (slope curvature of less than $-2\,m^{-1}$), and the values are 24.86 and 19.38 landslides km^{-2}, 1.707 %, and 27.79 mm. If we only divide the classes by the absolute value of slope curvature (ignoring if the slopes are convex or concave), it is clear that landslide occurred much less on flat-surface slopes (Fig. 20b).

Topographic position may also be a controlling parameter of co-seismic landslides. It is generally classified into six classes including ridges, upper slopes, middle slopes, flat

slopes, lower slopes, and valleys (Weiss, 2001). More recently, Jenness et al. (2013) renamed some of the categories and developed an extension to be analyzed with ArcGIS. In this work, the study area were classified into six categories, including valleys, lower slopes, gentle slopes, steep slopes, upper slopes, and ridges based on the extension and the DEM of the study area. The correlations of the classes, areas of classes, and LCND, LTND, LAP, and LET values are shown in Fig. 21. Most of the study area belongs to the class of steep slopes. It should be noted that the definition of steep slopes of topographic position in this study is not exactly the same as conventional definition of steep slopes that is based on slope angle (Fig. 18). The classification of topographic position of a cell in DEM takes into account not only the slope angles, but also the average elevations of the neighboring cells. Therefore, although the slope angles of most study area are less than 30°, the topographic position class of steep slopes covers the largest area. None of LCND, LPND, LAP, or LET show obvious correlations with topographic position. In general, valleys and lower slopes have higher values of the four proxies, followed by steep slopes, upper slopes, and ridges. This perhaps because the downcutting of rivers may cause the lower slopes to be unstable and loose deposits and weathered materials often accumulate in areas of valleys and lower slopes. Such correlations also appeared in some other earthquake events, such as the 2008 Wenchuan earthquake (Xu et al., 2014) and the 2010 Yushu earthquake (Xu et al., 2013a). The LCND values are slightly higher than the LTND values in valleys and lower slopes, but are the opposite in upper slopes and ridges. This corresponds to the locations of the top points and centroids of a landslide.

Co-seismic landslides mostly occur along rivers. This perhaps because (i) the downcutting of rivers results in many unvegetated steep slopes that are prone to co-seismic landslides; (ii) a lot of loose slope materials accumulate near the drainages and are prone to failure during strong ground shaking. The drainages of the study area are delineated from high-resolution satellite images and DEM. In order to correlate co-seismic landslides with distance from drainages, we first constructed zones with 100 m distance intervals from the drainages. Then, we divided ten classes of distance from

drainages, including 1: 0–100 m, 2: 100–200 m, 3: 200–300 m, 4: 300–400 m, 5: 400–500 m, 6: 500–600 m, 7: 600–700 m, 8: 700–800 m, 9: 800–900 m, 10: 900–1000 m, and 11: > 1000 m. The map of the zones was then converted into a raster map with 5 m resolution. Correlations of distance from drainages with LCND, LTND, LAP, and LET values are shown in Fig. 22. The results show that landslide abundance values decrease as distance from drainages increase. At the first three classes (0–300 m distance from the drainages), the four proxies of landslide abundance show a rapid decrease, and the values decrease slowly at other classes. This pattern indicates a strong control of the drainages for co-seismic landslides that are close to the drainages. All of the maximum values of LCND, LTND, LAP, and LET occur at 0–100 m distance from drainages. The values are 21.16 and 18.94 landslides km^{-2}, 1.222 %, and 23.47 mm. The centroid of a landslide is always closer to the drainages than its top point, thus the LCND value is higher than the LTND value at the class of 0–100 m distance from drainages. The two controlling parameters of topographic position and distance from drainages have somewhat similar meanings. For example, valleys have short distance from drainages and ridges mean long distance from drainages. Therefore, the correlations of co-seismic landslides with distance from drainages are similar to that with topographic position.

5.2 Lithology

Lithology is generally considered to play important roles in co-seismic landslide occurrence. The study area is covered by two major lithology groups, including sedimentary rocks and igneous rocks (Fig. 2). Most of the study area is covered by sedimentary rocks (about 2373 km^2, 74.3 % of the study area). The class 8 (Ems) covers the largest area (about 1010 km^2, 34.4 % of the study area), followed by class 14 (Cb), which covers about 749 km^2, about 23.5 % of the study area. The four co-seismic landslide abundance proxies show different patterns corresponding with the 14 classes of lithology (Fig. 23). The class 11 (Cs) has the highest LAP and LET values, which are 1.746 % and 38.43 mm. This is followed by classes 5 and 13 (Mi and Ca), which show 0.84 %

and 17.1 mm, 0.72 % and 9.9 mm, respectively. For the LCND and LTND values, both classes 11 and 13 (Cs and Ca) have similar maximum values: 25.31 and 25.34 landslides km^{-2} for class 11 (Cs), and 25.04 and 24.94 landslides km^{-2} for class 13 (Ca). They are followed by class 5 (Mi), with 19.77 and 19.79 landslides km^{-2}. Although class 8 (Ems) does not have high numbers of the landslide proxies, due to its large class area, total landslide numbers (10 702 and 10 696 landslides based on centroid and top point), area (6.06 km^2), and erosion volume (about 11 769 000 m^3) of the class are the highest.

5.3 Earthquake parameters

In order to carry out statistics of co-seismic landslide spatial distributions and earthquake parameters, we selected four parameters, including distance from the epicenter, distance from the Enriquillo–Plantain Garden fault, distance along the Enriquillo–Plantain Garden fault from the epicenter, and peak ground acceleration (PGA). We constructed zones with 2 km distance intervals from the epicenter (18°27′25″ N, 72°31′59″ W, NIEC, 2010) for the study area. The vector format map of the zones was converted into a raster map with 5 m resolution for the subsequent statistical analysis. The study area was divided into 28 classes. As shown in Fig. 24, the four proxies of landslide abundance are generally higher at classes 1–15 (less than 30 km from the epicenter) than at classes 16–28 (more than 30 km from the epicenter). However, the pattern does not show continuous decrease with increasing distance from the epicenter. The maximum values of LCND and LTND occur at class 1 (0–2 km from the epicenter), with the values of 25.56 landslides km^{-2}. The maximum values of LAP and LET, however, appear at class 9 (16–18 km from the epicenter), with values of 1.101 % and 22.57 mm. The four indexes show differences in different classes. This indicates that the scales of co-seismic landslides are controlled by the distance from the epicenter. The sharp drop of the values of the four indexes suggests the earthquake energy decay notably at about 30 km away from the epicenter.

Several previous studies (e.g., Calais et al., 2010; Hayes et al., 2010; Prentice et al., 2010) suggested that instead of the Enriquillo–Plantain Garden fault, a blind fault named the Léogâne fault is the actual seismogenic fault of the earthquake. Since (i) the exact location of the Léogâne fault is unclear due to no obvious geomorphic expression of the fault; (ii) the Léogâne fault is suggested to be only a few km north of and sub-parallel to the Enriquillo–Plantain Garden fault, we decided to still use the Enriquillo–Plantain Garden fault to carry out statistical analysis of co-seismic landslides with distance from the seismogenic fault. Furthermore, the geometry of the two faults implies that the blind Léogâne fault is a branch of the Enriquillo–Plantain Garden fault and the Enriquillo–Plantain Garden fault may still play important roles for the Haiti earthquake. The band width was set to be 1 km distance from the fault. The outer bands with no co-seismic landslide were combined with their neighboring bands. As a result, there are 7 bands in the northern block and 32 bands in the southern block of the Enriquillo–Plantain Garden fault. Figure 25 shows the correlations of areas of classes, and LCND, LPND, LAP, and LET values with the distance from the fault. In Fig. 25a, we analyzed without considering the differences of the southern or northern blocks, whereas in Fig. 25b, the two blocks were analyzed separately. In Fig. 25a, the maximum values of LCND, LPND, LAP, and LET, found at class 1 (0–1 km to the fault), are 22.85 and 22.82 landslides km^{-2}, 1.356 %, and 27.19 mm. Except for a sudden increase at classes 11 and 12 (10–12 km to the fault), the four indexes generally decrease with increasing distance from the fault. As shown in Fig. 25b, most of the co-seismic landslides (28 323 landslides covering about 1.15 km^2, 91.9 % of the total landslide number and 92.7 % of the total landslide area) occurred in the southern block of the fault. A similar decreasing trend of landslide abundance with increasing distance to the fault, similar to Fig. 25a, is present. The maximum values of the four indexes (25.49 and 25.39 landslides km^{-2}, 1.724 %, and 33.96 mm) occur at class 32 (0–1 km from the fault in the southern block). On the other hand, landslides at classes 1 and 2 show higher LAP and LET but lower LCND and LTND (Fig. 25a). This indicates that

larger co-seismic landslides are relatively abundant near the Enriquillo–Plantain Garden fault (within 4 km from the fault).

The geometrical characteristics of seismogenic faults usually influence the distribution of co-seismic landslides (Xu et al., 2013b; Gorum et al., 2011). The Enriquillo–Plantain Garden fault can be divided into five segments (Fig. 26), including the Miragoane, Goave, Dufort, Momance, and Dumay segment from west to east (Prentice et al., 2010). In order to assess co-seismic landslide abundance changes along different segments of the fault, a map of 2 km wide bands perpendicular to the fault on both sides of the epicenter was produced (Fig. 26). As a result, the study area is divided into 47 classes from west to east and the epicenter is located at between classes 26 and 27. There are 25 bands west of the epicenter and 22 bands east of the epicenter. Figure 26 also shows the correlations of the co-seismic landslides with the distance along the Enriquillo–Plantain Garden fault. Three areas of obvious high co-seismic landslide concentration are present at 22–26 km west to the epicenter (classes 13–15), 8–12 km west to the epicenter (classes 20 and 21), and 6–18 km east to the epicenter (classes 29–34). The Goave and Momance segments correspond to more co-seismic landslides than the other three segments. These results show that the co-seismic landslide occurrence was obviously different along different segments of the fault. The maximum values of LCND and LTND occur at class 21 (8–10 km west of the epicenter), which are 31.88 and 31.87 landslides km^{-2}, whereas the maximum values of LAP and LET occur at class 14 (22–24 km west of the epicenter), which are 1.7.92 % and 36.06 mm. The LCND and LTND values at class 14 are 30.37 and 30.31 landslides km^{-2}, slightly less than those at class 21. Such differences of the co-seismic landslides may result from local site effects such as geology, lithology, and topography, but they are more likely produced by differences of different segments of the fault. More detailed analyses of the segments of the Enriquillo–Plantain Garden fault are needed in order to test this hypothesis.

In general, there is a good correlation between distribution of co-seismic landslides and peak ground acceleration (PGA). The PGA data of the Haiti earthquake is obtained

from the US Geological Survey (2010). Range of the PGA values of the study area is from 0.12 g to 0.7 g with a 0.04 g interval (Fig. 27). There are nine classes of PGA of the study area, including 1: ≤ 0.16 g, 2: 0.2 g, 3: 0.24 g, 4: 0.28 g, 5: 0.32 g, 6: 0.36 g, 7: 0.4 g, 8: 0.44 g, and 9: ≥ 0.48 g. Figure 27 also shows the correlations of PGA values with the co-seismic landslide abundances. Except for class 9 (PGA ≥ 0.48 g), the LCND, LTND, LAP, and LET values show increasing trends with increasing PGA values. Although the area around Léogâne (Figs. 10 and 27) is covered by PGA values of ≥ 0.48 g, the co-seismic landslide abundances are quite low there due to the area is a plain area with gentle topography. Perhaps class 8 (0.44 g) is also partly affected by the gentle topography. The sudden increase of the four co-seismic landslide indexes from class 3 (0.24 g) to class 4 (0.28 g) indicates a sudden increase of ability to trigger many co-seismic landslides at PGA values of 0.24–0.28 g in the study area. Values of the four co-seismic landslide proxies at classes 1–4 (≤ 0.28 g) show similar trends, whereas they show different patterns at classes 5–8 (0.32–0.44 g). This suggests that the distributions of different scaled co-seismic landslides at classes 5–8 are uneven. The maximum LCND and LTND values occur at class 8 (0.44 g), which are 23.18 and 23.39 landslides km^{-2}, whereas the maximum LAP and LET values occur at class 7 (0.4 g), which are 1.131 % and 20.79 mm.

6 Controls of the impact parameters on co-seismic landslides

A simple bivariate statistical method can be used to compare the controls of impact parameters on co-seismic landslides occurrence (Xu and Xu, 2014; Xu et al., 2014). Based on this method, a percentage related to an impact parameter of co-seismic landslides can be derived, and this percentage indicates the spatial intensity of landslides related to that impact parameter. For example, when constructing the percentage curve related to slope angle and co-seismic landslide area, we plot the horizontal axis as the cumulative percentage of class area, and the vertical axis as the corresponding cumulative percentage of co-seismic landslide area (landslide area in a class divided by

the total landslide area). The area percentage under this curve would then represent the controlling degree of the impact parameter on co-seismic landslides area. If the co-seismic landslide area is only slightly controlled by a parameter, the curve would appear as a straight line and the area percentage under the curve would be close to 50 %. In the contrary, if co-seismic landslides were strongly controlled by a parameter, the curve would be a convex curve and the area percentage under the curve would be greater than 50 %. In an extreme case that the landslides are entirely controlled by one impact factor, the area of all landslides would be totally coincident with one class of that impact parameter. Under such circumstances, the influence percentage value of that factor can be calculated using the following equation:

$$P = 100\% - (0.5 \times L/A) \times 100\% \quad (2)$$

where P is the influence percentage on co-seismic landslides of that parameter, L is the total landslide area, and A is the total area of the study area. For any parameter of the Haiti earthquake, the P is "100 % – (0.5 × 15.736/3192.85) × 100 %", which is about 99.75 %. Of course, such ideal situation does not exist in reality.

In this study, 28 curves were constructed for the 4 co-seismic landslide proxies (LCND, LTND, LAP, and LET) and 7 co-seismic landslide impact parameters (slope angle, slope curvature, distance from epicenter, distance from the Enriquillo–Plantain Garden fault, PGA, distance from drainages, and lithology). The results were shown in Table 3 and Figs. 28 and 38. In Fig. 28, the 28 curves were separately shown in 7 figures base on the 7 impact parameters in order to see the differences between the 4 co-seismic landslide proxies. We found that the 4 curves related to most of the impact parameters show similar trends. Only the curves related to slope angle show clear difference between the 4 proxies. Therefore, we suggest that slope angle has highest control of landslide scales triggered by the Haiti-earthquake, even though this phenomenon is not easily observable in Fig. 18. In Fig. 29, the 28 curves were separately shown in 4 figures based upon the 4 co-seismic landslide proxies. We can observe in this figure that the area percentage under the curve of slope angle is the highest

no matter which proxy is selected. This result also suggests that the Haiti earthquake-triggered landslides were mostly controlled by slope angle. This method, however, has two limitations: (i) the co-seismic landslide impact parameters are assumed to be independent from one another, and (ii) the results may be affected by the selection of the study area.

7 Analysis and discussions

For the 2010 Haiti earthquake, Jibson and Harp (2011) firstly estimated that the earthquake would trigger 4000–5000 landslides by an empirical function of earthquake magnitudes and earthquake-triggered landslides worldwide (Keefer, 2002; Malamud et al., 2004). Subsequently, Harp et al. (2013) reported that at least 7000 landslides were triggered by this earthquake. Recently, Gorum et al. (2013) delineated 4490 landslides triggered by the Haiti earthquake. In this study, based on a thorough analysis of high-resolution satellite images, we detected 30 828 co-seismic landslides and prepared a new and much more comprehensive co-seismic landslide inventory related to the Haiti earthquake. However, we try to analyze the reasons of such obvious difference from other aspects.

There may be several different reasons for such a large difference in the number of detected co-seismic landslides. In this study, several principles are used: (i) all landslides were delineated as polygons, including very small landslides as long as they can be recognized in the images. (ii) The landslide complexes were separated into individual landslides. (iii) If a landslide exists on both pre- and post-earthquake images, it is considered a pre-existing landslide only if its shape remained the same in both images. Otherwise the landslide is considered a co-seismic landslide. In previous point-based landslide inventories (Jibson and Harp, 2011; Harp et al., 2013), small-scaled landslides may have been overlooked since the co-seismic landslides have very high density, so that it is very difficult to pick up all co-seismic landslides. A polygon-based inventory would be better in this aspect. However, Gorum et al. (2013) used polygons to

represent landslides but still reported only 4490 co-seismic landslides. We suspected that there are three possible reasons for this difference: (i) there may be coalescing landslide complexes that were not separated into individual landslides; (ii) co-seismic landslides occurred on old landslide slopes (landslides show different shapes on pre- and post-earthquake satellite images) may have been considered as pre-earthquake landslides; (iii) small-scaled landslides may have been ignored.

The situation where small-scaled landslides were overlooked can also be observed by the landslide area and number distribution curve (Fig. 13). In this study, the curve bends and drops at about 100 m^2 of landslide area, but the curve of the co-seismic landslide inventory by Gorum et al. (2013) bends and drops at about 1000 m^2 of landslide area. This indicates many co-seismic landslides of area less than 1000 m^2 were not included or were delineated as landslide complexes. The 1 km × 1 km grid of the largest landslide number, landslide area and landslide volume (Fig. 11) also show the high density of the Haiti earthquake-triggered landslides. The largest values of LND, LAP, and LET based on the 1 km × 1 km grids are 349 landslides km^{-2}, 24.42 %, and 679.7 mm. The correlations of the maximum values and distribution area (or number of 1 km × 1 km grids) were shown in Fig. 30. The universal power laws between landslide abundances per 1 km^2 (LND, LAP, and LET) and the cumulative area (cumulative number of 1 km × 1 km grids) were shown in Fig. 30a–c. The very few abnormalities in Fig. 30 indicate the completeness of the inventory of landslides triggered by the Haiti earthquake.

It is noteworthy that only 4000–5000 landslides should have been triggered by the Haiti earthquake based on calculations of the empirical function of earthquake magnitude and earthquake-triggered landslides worldwide (Keefer, 2002; Malamud et al., 2004; Jibson and Harp, 2011). Much more co-seismic landslides were detected in this study. Two major reasons are responsible for this difference: (i) the recent availability of very high resolution (about 0.5 m) satellite images enabled much more detailed co-seismic landslide analysis. (ii) New principles of co-seismic landslides interpretation (e.g., co-seismic landslides should be delineated as long as they can be recognized

on images; landslides complexes should be separated into individual landslides) were proposed and the completeness of co-seismic landslide inventories is significantly improved. Therefore, it may be necessary to update the empirical functions based on more and more new and complete co-seismic landslide data that become available recently.

8 Conclusions

In this paper, we conducted a detailed visual interpretation of landslides triggered by the 2010 Haiti earthquake. The results show that at least 30 828 landslides were triggered by the earthquake. These landslides distributed in an area larger than 3000 km^2, and covered about 15.736 km^2, with an estimated landslide erosion volume about 29 700 000 m^3. Spatial distribution maps and contour maps of landslide number density, landslide area percentage, and landslide erosion thickness were constructed respectively in order to analyze the spatial distribution patterns of the co-seismic landslides. Two ellipsoid-shaped areas of high co-seismic landslide density are present. One is located east of the epicenter, showing an east–west trending long axis, and the epicenter is located at about the west end of this long axis. The other area is located about 20 km southwest of the epicenter and its long axis has northwest–southeast trending. Four co-seismic landslide abundance proxies, including landslide centroid number density (LCND), landslide top number density (LTND), landslide area percentage (LAP), and landslide erosion thickness (LET) were used to correlate the co-seismic landslides with landslide controlling parameters. Statistical results show that there are generally positive correlations between co-seismic landslides and slope angle and PGA, and generally negative correlations with the distance from the Enriquillo–Plantain Garden fault. Co-seismic landslide abundances with the distance along the fault show that the Goave and Momance segments of the fault correspond to more landslides. As slope curvature values gets closer to zero, the number of co-seismic landslides decreases. The elevation range of high landslide susceptibility is between 200 m and 1200 m. The co-seismic

landslides occurred preferably on east oriented slopes, since this corresponds with the movement direction of the curst of most study area. The co-seismic landslides show different abundances in different lithology classes, but most of the landslides occurred within 30 km from the epicenter. Slope angle may have the strongest control on the Haiti earthquake-triggered landslides. Since many detailed and more complete co-seismic landslide inventories become available with the recent availability of high-resolution remote sensing datasets, it may be necessary to update the empirical functions based on these new co-seismic landslide data.

Acknowledgements. This research was supported by the National Science Foundation of China (41202235 and 91214201), the National Science Council (NSC) of Taiwan (NSC 102-2811-M-002-063 and 102-2628-M-002-007-MY3 to J.B.H.S.), and the Basic Scientific Fund of the Institute of Geology, China Earthquake Administration (IGCEA1215, IGCEA1302). Satellite images in this study are from the Google Earth platform.

References

Adams, J.: Contemporary uplift and erosion of the Southern Alps, New Zealand, Geol. Soc. Am. Bull., 91, 1–114, 1980.

Alfaro, P., Delgado, J., García-Tortosa, F., Lenti, L., López, J., López-Casado, C., and Martino, S.: Widespread landslides induced by the Mw 5.1 earthquake of 11 May 2011 in Lorca, SE Spain, Eng. Geol., 137–138, 40–52, 2012.

Ali, S. T., Freed, A. M., Calais, E., Manaker, D. M., and McCann, W. R.: Coulomb stress evolution in Northeastern Caribbean over the past 250 yr due to coseismic, postseismic and interseismic deformation, Geophys. J. Int., 174, 904–918, 2008.

Agnesi, V., Camarda, M., Conoscenti, C., Di Maggio, C., Diliberto, I. S., Madonia, P., and Rotigliano, E.: A multidisciplinary approach to the evaluation of the mechanism that triggered the Cerda landslide (Sicily, Italy), Geomorphology, 65, 101–116, 2005.

Árnadóttir, T. and Segall, P.: The 1989 Loma Prieta earthquake imaged from inversion of geodetic data, J. Geophys. Res.-Sol. Ea., 99, 21835–21855, 1994.

Basharat, M., Rohn, J., Baig, M. S., and Khan, M. R.: Spatial distribution analysis of mass movements triggered by the 2005 Kashmir earthquake in the Northeast Himalayas of Pakistan, Geomorphology, 206, 203–214, doi:10.1016/j.geomorph.2013.09.025, 2014.

Bellerive, J. M.: Haiti Earthquake PDNA: assessment of damage, losses, general and sectoral needs, annex to the action plan for national recovery and development of Haiti, 114 pp., 2010.

Bilham, R.: Lessons from the Haiti earthquake, Nature, 463, 878–879, 2010.

Calais, E. and de Lépinay, B. M.: From transtension to transpression along the northern Caribbean plate boundary off Cuba: implications for the recent motion of the Caribbean plate, Tectonophysics, 1986, 329–350, 1991.

Calais, E., Béthoux, N., and de Lépinay, B. M.: From transcurrent faulting to frontal subduction: a seismotectonic study of the Northern Caribbean Plate Boundary from Cuba to Puerto Rico, Tectonics, 11, 114–123, 1992.

Calais, E., Perrot, J., and de Lépinay, B. M.: Strike-slip tectonics and seismicity along the northern Caribbean plate boundary from Cuba to Hispaniola, Geol. S. Am. S., 326, 125–169, 1998.

Calais, E., Freed, A., Mattioli, G., Amelung, F., Jónsson, S., Jansma, P., Hong, S. H., Dixon, T., Prépetit, C., and Momplaisir, R.: Transpressional rupture of an unmapped fault during the 2010 Haiti earthquake, Nat. Geosci., 3, 794–799, 2010.

Carro, M., De Amicis, M., Luzi, L., and Marzorati, S.: The application of predictive modeling techniques to landslides induced by earthquakes: the case study of the 26 September 1997 Umbria–Marche earthquake (Italy), Eng. Geol., 69, 139–159, 2003.

Chen, X. L., Yu, L., Wang, M. M., and Li, J. Y.: Brief Communication: Landslides triggered by the Ms = 7.0 Lushan earthquake, China, Nat. Hazards Earth Syst. Sci. Discuss., 1, 3891–3918, doi:10.5194/nhessd-1-3891-2013, 2013.

Chigira, M. and Yagi, H.: Geological and geomorphological characteristics of landslides triggered by the 2004 Mid Niigta prefecture earthquake in Japan, Eng. Geol., 82, 202–221, 2006.

Collins, B. D., Kayen, R., and Tanaka, Y.: Spatial distribution of landslides triggered from the 2007 Niigata Chuetsu-Oki Japan Earthquake, Eng. Geol., 127, 14–26, 2012.

Dai, F. C., Xu, C., Yao, X., Xu, L., Tu, X. B., and Gong, Q. M.: Spatial distribution of landslides triggered by the 2008 Ms 8.0 Wenchuan earthquake, China, J. Asian Earth Sci., 40, 883–895, 2011.

de Lépinay, B. M., Deschamps, A., Klingelhoefer, F., Mazabraud, Y., Delouis, B., Clouard, V., Hello, Y., Crozon, J., Marcaillou, B., and Graindorge, D.: The 2010 Haiti earthquake: a complex fault pattern constrained by seismologic and tectonic observations, Geophys. Res. Lett., 38, L22305, doi:10.1029/2011GL049799, 2011.

DeMets, C., Jansma, P. E., Mattioli, G. S., Dixon, T. H., Farina, F., Bilham, R., Calais, E., and Mann, P.: GPS geodetic constraints on Caribbean–North America plate motion, Geophys. Res. Lett., 27, 437–440, 2000.

DesRoches, R., Comerio, M., Eberhard, M., Mooney, W., and Rix, G. J.: Overview of the 2010 Haiti earthquake, Earthq. Spectra, 27, S1–S21, 2011.

Dixon, T. H., Farina, F., DeMets, C., Jansma, P., Mann, P., and Calais, E.: Relative motion between the Caribbean and North American plates and related boundary zone deformation from a decade of GPS observations, J. Geophys. Res., 103, 15157–15182, 1998.

Eberhard, M. O., Baldridge, S., Marshall, J., Mooney, W., and Rix, G. J.: The Mw 7.0 Haiti Earthquake of 12 January 2010: USGS/EERI Advance Reconnaissance Team Report, US Geological Survey Open-File Report 2010–1048, 58 pp., available at: http://pubs.usgs.gov/of/2010/1048, 2010.

Frankel, A., Harmsen, S., Mueller, C., Calais, E., and Haase, J.: Documentation for Initial Seismic Hazard Maps for Haiti, US Geological Survey, Open File Report 2010–1067, 12 pp., available at: http://pubs.usgs.gov/of/2010/1067, 2010.

Fukuoka, H., Sassa, K., and Scarascia-Mugnozza, G.: Distribution of landslides triggered by the 1995 Hyogo-ken Nanbu earthquake and long runout mechanism of the Takarazuka Golf Course landslide, J. Phys. Earth, 45, 83–90, 1997.

Gorum, T., Fan, X. M., van Westen, C. J., Huang, R. Q., Xu, Q., Tang, C., and Wang, G. H., Distribution pattern of earthquake-induced landslides triggered by the 12 May 2008 Wenchuan earthquake, Geomorphology, 133, 152–167, 2011.

Gorum, T., van Westen, C. J., Korup, O., van der Meijde, M., Fan, X. M., and van der Meer, F. D.: Complex rupture mechanism and topography control symmetry of mass-wasting pattern, 2010 Haiti earthquake, Geomorphology, 184, 127–138, 2013.

Guzzetti, F., Mondini, A. C., Cardinali M, Fiorucci, F., Santangelo, M., and Chang, K. T.: Landslide inventory maps: new tools for an old problem, Earth-Sci. Rev., 112, 42–66, 2012.

Harp, E. L. and Jibson, R. W.: Inventory of landslides triggered by the 1994 Northridge, California earthquake, US Geological Survey, available at: http://geo-nsdi.er.usgs.gov/metadata/open-file/95-213, 1995.

Harp, E. L. and Jibson, R. W.: Landslides triggered by the 1994 Northridge, California, Earthquake, B. Seismol. Soc. Am., 86, S319–S332, 1996.
Harp, E. L., Keefer, D. K., Sato, H. P., and Yagi, H.: Landslide inventories: the essential part of seismic landslide hazard analyses, Eng. Geol., 122, 9–21, 2011.
Harp, E. L., Jibson, R. W., and Dart, R. L.: The effect of complex fault rupture on the distribution of landslides triggered by the 12 January 2010, Haiti earthquake, Landslide Science and Practice, 5, 157–161, 2013.
Hashimoto, M., Fukushima, Y., and Fukahata, Y.: Fan-delta uplift and mountain subsidence during the Haiti 2010 earthquake, Nat. Geosci., 4, 255–259, 2011.
Hayes, G. P., Briggs, R. W., Sladen, A., Fielding, E. J., Prentice, C., Hudnut, K., Mann, P., Taylor, F. W., Crone, A. J., Gold, R., Ito, T., and Simons, M.: Complex rupture during the 12 January 2010 Haiti earthquake, Nat. Geosci., 3, 800–805, 2010.
Hough, S. E., Altidor, J. R., Anglade, D., Given, D., Janvier, M. G., Maharrey, J. Z., Meremonte, M., Mildor, B. S. L., Prepetit, C., and Yong, A.: Localized damage caused by topographic amplification during the 2010 M 7.0 Haiti earthquake, Nat. Geosci., 3, 778–782, 2010.
Jenness, J., Brost, B., and Beier, P.: Land Facet Corridor Designer: Topographic Position Index Tools, available at: http://www.jennessent.com, 2013.
Jibson, R. W. and Harp, E. L.: Landslides triggered by the Northridge Earthquake, Earthquake and Volcanoes, 25, 31–41, 1994.
Jibson, R. W. and Harp, E. L.: Field reconnaissance report of landslides triggered by the 12 January 2010, Haiti earthquake, Open-File Report 2011–1023, 19 pp., available at: http://pubs.usgs.gov/of/2011/1023, 2011.
Jibson, R. W. and Harp, E. L.: Extraordinary distance limits of landslides triggered by the 2011 Mineral, Virginia, earthquake, B. Seismol. Soc. Am., 102, 2368–2377, 2012.
Jibson, R. W., Harp, E. L., Schulz, W., Keefer, D. K.: Landslides triggered by the 2002 Denali Fault, Alaska, earthquake and the inferred nature of the strong shaking, Earthq. Spectra, 20, 669–691, 2004.
Kamp, U., Growley, B. J., Khattak, G. A., and Owen, L. A.: GIS-based landslide susceptibility mapping for the 2005 Kashmir earthquake region, Geomorphology, 101, 631–642, 2008.
Keefer, D. K.: Landslides caused by earthquakes, Geol. Soc. Am. Bull., 95, 406–421, 1984.
Keefer, D. K.: The importance of earthquake-induced landslides to long-term slope erosion and slope-failure hazards in seismically active regions, Geomorphology, 10, 265–284, 1994.

Keefer, D. K.: Earthquake-induced landslides and their effects on alluvial fans, J. Sediment. Res., 69, 84–104, 1999.
Keefer, D. K.: Statistical analysis of an earthquake-induced landslide distribution – the 1989 Loma Prieta, California event, Eng. Geol., 58, 231–249, 2000.
Keefer, D. K.: Investigating landslides caused by earthquakes – a historical review, Surv. Geophys., 23, 473–510, 2002.
Keefer, D. K., Wilson, R. C., Harp, E. L., and Lips, E. W.: The Borah Peak, Idaho earthquake of 28 October 1983 – landslides, Earthq. Spectra, 2, 91–125, 1985.
Keefer, D. K., Wartman, J., Ochoa, C. N., Rodriguez-Marek, A., and Wieczorek, G. F.: Landslides caused by the M 7.6 Tecomán, Mexico earthquake of 21 January 2003, Eng. Geol., 86, 183–197, 2006.
Khazai, B. and Sitar, N.: Evaluation of factors controlling earthquake-induced landslides caused by Chi-Chi earthquake and comparison with the Northridge and Loma Prieta events, Eng. Geol., 71, 79–95, 2004.
Koehler, R. D. and Mann, P.: Field observations from the 12 January 2010, Haiti earthquake: implications for seismic hazards and future post-earthquake reconnaissance investigations in Alaska, Report of Investigations 2011-2, 24 pp., available at: http://www.dggs.alaska.gov/webpubs/dggs/ri/text/ri2011_002.pdf, 2011.
Lambert, M. L., Gaudin, J., and Cohen, R.: Carte Geologique D'Haiti, Feuille Sud-Est: Port-au-Prince, 1 : 250 000, C.E.R.C.G.IMAGEO.C.N.R.S. 191 rue Saint Jacques 75005, Paris, 1987 (Digital image and georeferencing: John Walker, Matraco-Colorado Holding Ltd, 2003).
Larsen, I. J., Montgomery, D. R., and Korup, O.: Landslide erosion controlled by hillslope material, Nat. Geosci., 3, 247–251, 2010.
Liao, H. W. and Lee, C. T.: Landslides triggered by the Chi-Chi earthquake, in: Proceedings of the 21st Asian Conference on Remote Sensing, Taipei, 1–2, 383–388, 2000.
Liao, C., Liao, H., and Lee, C.: Statistical analysis of factors affecting landslides triggered by the 1999 Chi-Chi earthquake, Taiwan, in: American Geophysical Union, Fall Meeting, abstract #H12D-0951, 2002.
Mahdavifar, M. R., Solaymani, S., and Jafari, M. K.: Landslides triggered by the Avaj, Iran earthquake of 22 June 2002, Eng. Geol., 86, 166–182, 2006.
Malamud, B. D., Turcotte, D. L., Guzzetti, F., and Reichenbach, P.: Landslide inventories and their statistical properties, Earth Surf. Proc. Land., 29, 687–711, 2004.

Manaker, D. M., Calais, E., Freed, A. M., Ali, S. T., Przybylski, P., Mattioli, G., Jansma, P., Prépetit, C., and De Chabalier, J. B.: Interseismic plate coupling and strain partitioning in the Northeastern Caribbean, Geophys. J. Int., 174, 889–903, 2008.
Mann, P., Burke, K., and Matumoto, T.: Neotectonics of Hispaniola: plate motion, sedimentation, and seismicity at a restraining bend, Earth Planet. Sc. Lett., 70, 311–324, 1984.
Mann, P., Taylor, F. W., Edwards, R. L., and Ku, T. L.: Actively evolving microplate formation by oblique collision and sideways motion along strike-slip faults: an example from the Northeastern Caribbean plate margin, Tectonophysics, 246, 1–69, 1995.
Mann, P., Calais, E., Ruegg, J. C., DeMets, C., Jansma, P. E., and Mattioli, G. S.: Oblique collision in the northeastern Caribbean from GPS measurements and geological observations, Tectonics, 21, 1057, doi:10.1029/2001TC001304, 2002.
Marzorati, S., Luzi, L., and Amicis, M. D.: Rock falls induced by earthquakes: a statistical approach, Soil Dyn. Earthq. Eng., 22, 565–577, 2002.
NEIC: National Earthquake Information Center [EB/OL], available at: http://earthquake.usgs.gov/regional/neic, 2010.
Owen, L. A., Kamp, U., Khattak, G. A., Harp, E. L., Keefer, D. K., and Bauer, M. A.: Landslides triggered by the 8 October 2005 Kashmir earthquake, Geomorphology, 94, 1–9, 2008.
Parker, R. N., Densmore, A. L., Rosser, N. J., de Michele, M., Li, Y., Huang, R. Q., Whadcoat, S., and Petley, D. N.: Mass wasting triggered by 2008 Wenchuan earthquake is greater than orogenic growth, Nat. Geosci., 4, 449–452, 2011.
Parise, M.: Erosion rates from seismically-induced landslides in Irpinia, Southern Italy, in: Proc. 8th Int. Symposium on Landslides, Cardiff, vol. 3, 1159–1164, 2000.
Parise, M. and Jibson, R. W.: A seismic landslide susceptibility rating of geologic units based on analysis of characteristics of landslides triggered by the 17 January 1994 Northridge, California earthquake, Eng. Geol., 58, 251–270, 2000.
Pearce, A. J. and O'Loughlin, C. L.: Landsliding during a M 7.7 earthquake: influence of geology and topography, Geology, 13, 855–858, 1985.
Prentice, C. S. and Schwartz, D. P.: Re-evaluation of 1906 surface faulting, geomorphic expression, and seismic hazard along the San Andreas fault in the Southern Santa Cruz Mountains, B. Seismol. Soc. Am., 81, 1424–1479, 1991.
Prentice, C., Mann, P., Crone, A., Gold, R., Hudnut, K., Briggs, R., Koehler, R., and Jean, P.: Seismic hazard of the Enriquillo–Plantain Garden fault in Haiti inferred from palaeoseismology, Nat. Geosci., 3, 789–793, 2010.

Qi, S. W., Xu, Q., Zhang, B., Zhou, Y. D., Lan, H., and Li, L. H.: Source characteristics of long runout rock avalanches triggered by the 2008 Wenchuan earthquake, China, J. Asian Earth Sci., 40, 896–906, 2011.
Rodríguez, C. E., Bommer, J. J., and Chandler, R. J.: Earthquake-induced landslides: 1980–1997, Soil Dyn. Earthq. Eng., 18, 325–346, 1999.
Sassa, K.: Landslide disasters triggered by the 2004 Mid-Niigata Prefecture earthquake in Japan, Landslides, 2, 135–142, 2005.
Sato, H. P., Sekiguchi, T., Kojiroi, R., Suzuki, Y., and Iida, M.: Overlaying landslides distribution on the earthquake source, geological and topographical data: the Mid Niigata prefecture earthquake in 2004, Japan, Landslides, 2, 143–152, 2005.
Sato, H. P., Hasegawa, H., Fujiwara, S., Tobita, M., Koarai, M., Une, H., and Iwahashi, J.: Interpretation of landslide distribution triggered by the 2005 Northern Pakistan earthquake using SPOT 5 imagery, Landslides, 4, 113–122, 2007.
Scherer, J.: Great earthquakes in the Island of Haiti, B. Seismol. Soc. Am., 2, 161–180, 1912.
Sekiguchi, T. and Sato, H. P.: Feature and distribution of landslides induced by the Mid Niigata Prefecture earthquake in 2004, Japan, Journal of the Japan Landslide Society, 43, 142–154, 2006.
Sepúlveda, S. A., Serey, A., Lara, M., Pavez, A., and Rebolledo, S.: Landslides induced by the April 2007 Aysén Fjord earthquake, Chilean Patagonia, Landslides, 7, 483–492, 2010.
Stumpf, A. and Kerle, N.: Object-oriented mapping of landslides using Random Forests, Remote Sens. Environ., 115, 2564–2577, 2011.
Tibaldi, A., Ferrari, L., and Pasquare, G.: Landslides triggered by earthquakes and their relations with faults and mountain slope geometry: an example from Ecuador, Geomorphology, 11, 215–226, 1995.
US Geological Survey: Shakemap us2010rja6 [EB/OL], available at: http://earthquake.usgs.gov/earthquakes/shakemap/global/shake/2010rja6/, 2010.
Wang, W. N., Nakamura, H., Tsuchiya, S., and Chen, C. C.: Distributions of landslides triggered by the Chi-Chi earthquake in Central Taiwan on 21 September 1999, Landslides, 38, 18–26, 2002.
Wang, H. B., Sassa, K., and Xu, W. Y.: Analysis of a spatial distribution of landslides triggered by the 2004 Chuetsu earthquakes of Niigata Prefecture, Japan, Nat. Hazards, 41, 43–60, 2007.

Wdowinski, S. and Hong, S. H.: Postseismic deformation following the 2010 Haiti earthquake: groundwater flow in response to a sudden uplift, University of Miami, Rosenstiel School of Marine and Atmospheric Science, 9 pp., available at: http://terrasar-x.dlr.de/papers_sci_meet_4/oral/HYD0746_wdowinski_hong.pdf, 2010.

Weiss, A. D.: Topographic position and landforms analysis, Poster presentation, ESRI User Conference, San Diego, CA, available at: http://www.jennessent.com/downloads/tpi-poster-tnc_18x22.pdf, 2001.

Xu, C.: Preparation of earthquake-triggered landslide inventory maps using remote sensing and GIS technologies: principles and case studies, Geoscience Frontiers, 2014.

Xu, C. and Xiao, J. Z.: Spatial analysis of landslides triggered by the 2013 Ms 7.0 Lushan earthquake: a case study of a typical rectangle area in the northeast of Taiping Town, Seismology and Geology, 35, 436–451, 2013 (in Chinese with English abstract).

Xu, C. and Xu, X. W.: Statistical analysis of landslides caused by the Mw 6.9 Yushu, China, earthquake of 14 April 2010, Nat. Hazards, doi:10.1007/s11069-014-1038-2, 2014.

Xu, C., Dai, F. C., and Yao, X.: Incidence number and affected area of Wenchuan earthquake-induced landslides, Science and Technology Review, 27, 79–81, 2009 (in Chinese with English Abstract).

Xu, C., Xu, X. W., and Yu, G. H.: Earthquake triggered landslide hazard mapping and validation related with the 2010 Port-au-Prince, Haiti earthquake, Disaster Advances, 5, 1297–1304, 2012.

Xu, C., Xu, X. W., and Yu, G. H.: Landslides triggered by slipping-fault-generated earthquake on a plateau: an example of the 14 April 2010, Ms 7.1, Yushu, China earthquake, Landslides, 10, 421–431, 2013a.

Xu, C., Xu, X. W., Yao, Q., and Wang, Y. Y.: GIS-based bivariate statistical modelling for earthquake-triggered landslides susceptibility mapping related to the 2008 Wenchuan earthquake, China, Q. J. Eng. Geol. Hydroge., 46, 221–236, 2013b.

Xu, C., Xu, X. W., Yao, X., and Dai, F. C.: Three (nearly) complete inventories of landslides triggered by the 12 May 2008 Wenchuan Mw 7.9 earthquake of China and their spatial distribution statistical analysis, Landslides, doi:10.1007/s10346-013-0404-6, 2014.

Yagi, H., Higaki, D., Yamamoto, M., and Yamasaki, T.: Distribution and characteristics of landslides induced by the Iwate-Miyagi Nairiku earthquake in 2008 in Tohoku District, Northeast Japan, Landslides, 6, 335–344, 2009.

Yamagishi, H. and Iwahashi, J.: Comparison between the two triggered landslides in Mid-Niigata, Japan by 13 July heavy rainfall and 23 October intensive earthquakes in 2004, Landslides, 4, 389–397, 2007.

Zhang, Y. S., Yao, X., Xiong, T. Y., Ma, Y. S., Hu, D. G., Yang, N., and Guo, C. B.: Rapid identification and emergency investigation of surface ruptures and geohazards induced by the Ms 7.1 Yushu earthquake, Acta Geol. Sin.-Engl., 84, 1315–1527, 2010.

Table 1. Regional co-seismic landslide inventories related to recent earthquakes based on field investigations, GIS, and remote sensing technologies.

Earthquake events	Date	Magnitude (Mw)	Type	Number	Area	Distribution area	References
Mineral, Virginia	23 Aug 2011	5.8	Points			33 400	Jibson and Harp (2012)
Lorca, SE Spain	11 May 2011	5.1	Points	> 250		~ 300	Alfaro et al. (2012)
Yushu, China	14 Apr 2010	6.9	Polygons	2036	1.194	> 1455	Xu et al. (2013a)
			Points	282			Zhang et al. (2010)
Iwate–Miyagi Nairiku, Japan	14 Jun 2008	6.9	Polygons	> 4161	10.2	~ 600	Yagi et al. (2009)
Wenchuan, China	12 May 2008	7.9	Polygons	> 197 481	1160	110 000	Xu et al. (2014)
			Polygons	73 367	565.8	13 800	Parker et al. (2011)
			Points	< 60 000		20 000	Gorum et al. (2011)
			Polygons	> 56 000	811	41 750	Dai et al. (2011)
			Polygons	> 48 000	711.8	~ 50 000	Xu et al. (2009)
Niigata Chuetsu-Oki, Japan	16 Jul 2007	6.6		~ 70–312		~ 181–332	Collins et al. (2012)
Aysén Fjord, Chile	21 Apr 2007	6.2	Polygons	538	17	~ 400	Sepúlveda et al. (2010)
Kashmir	8 Oct 2005	7.6	Polygons	1293		> 7,500	Owen et al. (2008)
			Points	2424		2800	Sato et al. (2007)
			Polygons	2252	61	~ 2550	Kamp et al. (2008)
			Points	1460			Basharat et al. (2014)
Mid-Niigata, Japan	23 Oct 2004	6.6	Polygons	1212	7.99	275	Wang et al. (2007)
				> 1000			Chigira and Yagi (2006)
				362			Sassa (2005)
				1353			Sato et al. (2005)
				4438			Sekiguchi and Sato (2006), Yamagishi and Iwahashi (2007)
Tecomán, Mexico	21 Jan 2003	7.6		Several hundreds			Keefer et al. (2006)
Denali fault, Alaska	3 Nov 2002	7.9	Points	1000–10 000		~ 9000	Jibson et al. (2004)
South Tyrrhenian Sea, Sicily, Italy	6 Sep 2002	5.7	Polygons				Agnesi et al. (2005)
Avaj, Iran	22 Jun 2002	6.5	Points	59		3600	Mahdavifar et al. (2006)
Chi-Chi, Taiwan	21 Sep 1999	7.6	Polygons	> 10 000	127.8	11 000	Khazai and Sitar (2004), Liao and Lee (2000), Liao et al. (2002)
			Polygons	> 20 000			Wang et al. (2002)
Umbria–Mare, Italy	26 Sep 1997	6.0	Polygons	~ 200			Marzorati et al. (2002), Carro et al. (2003)
Hyogo-Ken Nanbu, Japan	17 Jan 1995	6.9	Points	674		700	Fukuoka et al. (1997)
Northridge, California	17 Jan 1994	6.7	Polygons	11 000	23.8	10 000	Harp and Jibson, (1995, 1996), Jibson and Harp (1994)
Loma Prieta, California	17 Oct 1989	6.9	Points	1046		2000	Keefer (2000)
Ecuador	5 Mar 1987	7.0				2500	Tibaldi et al. (1995)
Borah Peak, Idaho	28 Oct 1983	6.9	Points	Several hundreds		4200	Keefer et al. (1985)
Murchison	17 Jun 1929	7.7	Polygons	> 7400	200	5000	Pearce and O'Loughlin (1985), Adams (1980)

Table 2. Landslide number and landslide number percentage in different angle of reach of three conditions, including area larger than 100 m^2, larger than 1000 m^2, and larger than 10 000 m^2.

Angle of reach	Number of area > 100 m^2	Number %	Number of area > 1000 m^2	Number %	Number of area > 10 000 m^2	Number %
< 5	1856	9.332	82	2.301	0	0
5–10	3887	19.543	337	9.456	2	1.942
10–15	3796	19.086	474	13.300	8	7.767
15–20	3179	15.984	593	16.639	12	11.650
20–25	2528	12.711	535	15.011	14	13.592
25–30	1927	9.689	532	14.927	25	24.272
30–35	1450	7.290	471	13.215	20	19.417
35–40	829	4.168	370	10.382	19	18.447
40–45	311	1.564	123	3.451	3	2.913
45–50	93	0.468	34	0.954	0	0
50–55	25	0.126	12	0.337	0	0
55–60	7	0.035	1	0.028	0	0
> 60	1	0.005	0	0	0	0
Total	19 889	100	3564	100	103	100

Table 3. Table of area under curve (AUC) values of landslide area and landslide number.

Landslide parameters/ proxies	1	2	3	4
A	75.119	69.329	70.507	79.301
B	54.252	53.449	53.296	54.914
C	66.156	68.438	68.436	64.972
D	63.364	63.364	63.363	63.107
E	65.477	67.034	67.037	64.849
F	64.772	62.402	61.712	65.263
G	65.61	63.68	63.694	68.118

A: slope angle, B: slope curvature, C: distance from epicenter, D: distance from the Enriquillo–Plantain Garden fault, E: PGA, and F: distance from drainages. 1: landslide area, 2: landslide centroid point number, 3: landslide top point number, and 4: landslide accumulation material volume.

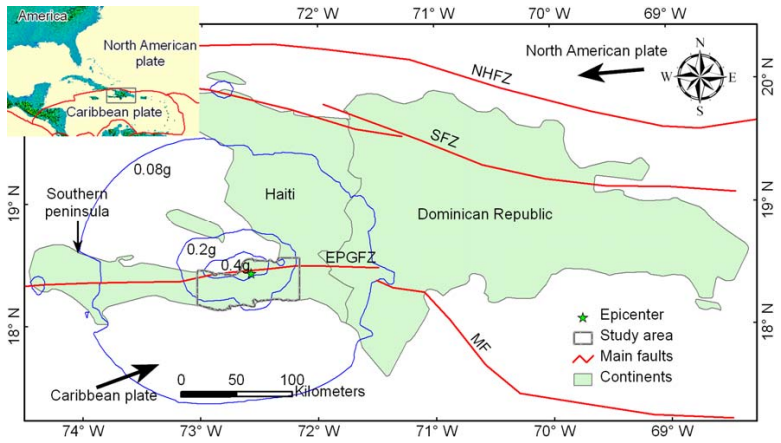

Fig. 1. Location of study area, shown by the gray polygon. Thin blue lines indicate generalized PGA value contour lines. NHFZ: North Hispaniola fault zone; SFZ: Septentrional fault zone; EPGFZ: the Enriquillo–Plantain Garden fault zone; MF: Muertos fault.

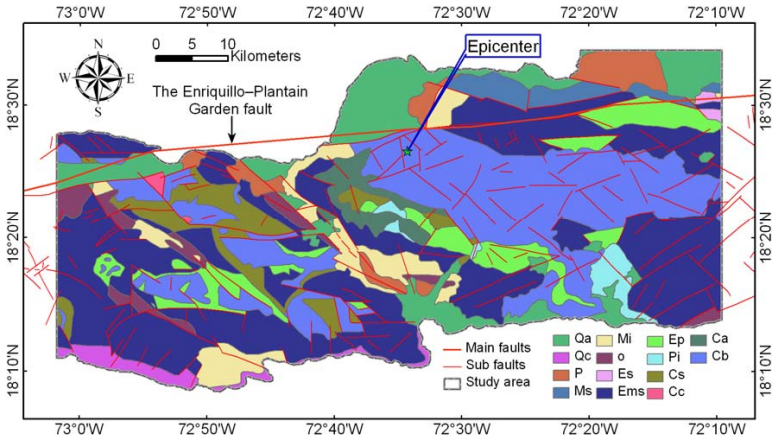

Fig. 2. The bedrock distribution map of the study area.

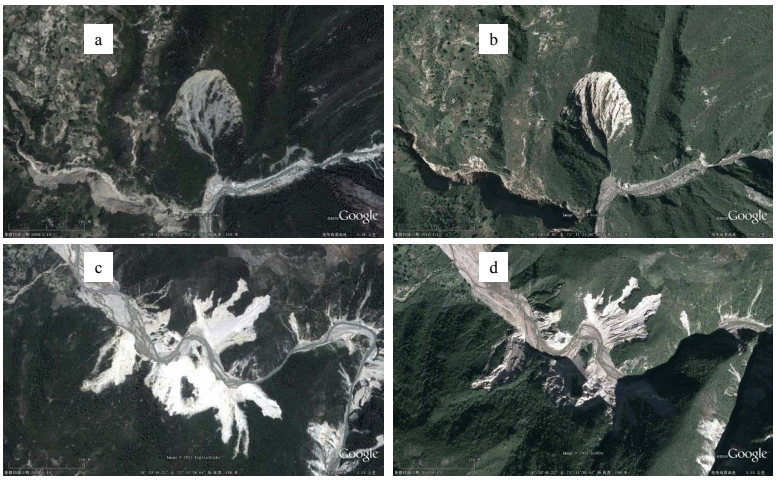

Fig. 3. Pre-earthquake landslides are shown in two locations. **(a)** and **(b)** is located at 18°29′02.70″ N, 72°11′22.28″ W; **(c)** and **(d)** is located at 18°29′46.48″ N, 72°11′37.86″ W. Images **(a)** and **(c)** were taken on 10 May 2008 and **(b)** and **(d)** were taken on 13 January 2010.

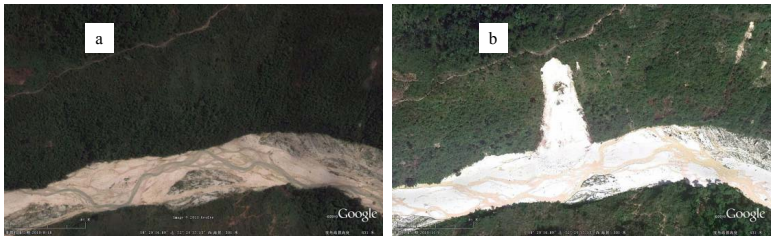

Fig. 4. A landslide (18°29′16.89″ N, 72°24′37.53″ W) occurred after the earthquake but may be triggered by rainfall. **(a)** was taken on 18 August 2010 and **(b)** was taken on 9 November 2010. Upward is north.

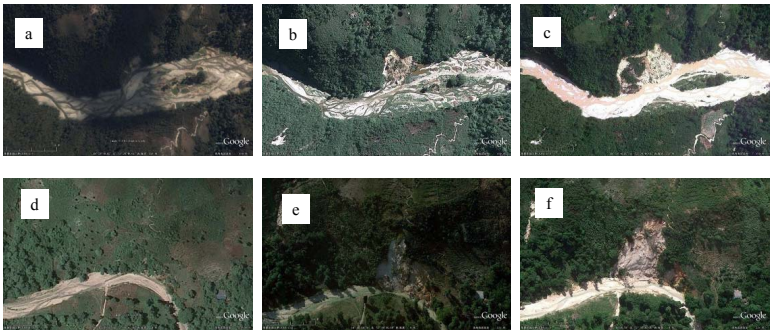

Fig. 5. Two places of co-seismic landslides probably enlarged by rainfall. **(a)**, **(b)**, and **(c)** are images showing a landslide located at 18°29′40.75″ N, 72°24′48.69″ W. The images were taken on 4 February 2009, 13 January 2010, and 9 November 2010, respectively. **(d)**, **(e)**, and **(f)** are images of a landslide located at 18°30′58.78″ N, 72°30′30.08″ W. The images were taken on 26 August 2009, 25 January 2010, and 9 November 2010, respectively.

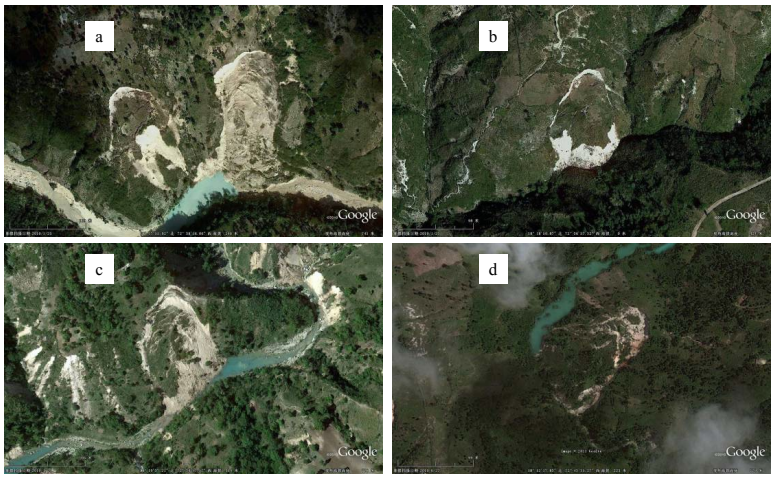

Fig. 6. Several typical co-seismic coherent deep-seated landslides. **(a)** Two coherent deep-seated landslides (18°17′54.15″ N, 72°38′18.95″ W) within a short distance. The image is taken on 25 January 2010 and upward is north. **(b)** is located at 18°18′50.87″ N, 72°36′57.32″ W, and the image was taken on 25 January 2010 and upward is north. **(c)** is located at 18°19′37.21″ N, 72°39′47.57″ W. The image is taken on 25 January 2010 and upward is west. **(d)** The landslide is located at 18°12′17.83″ N, 72°43′35.27″ W and the image is taken on 27 June 2010 and upward is north.

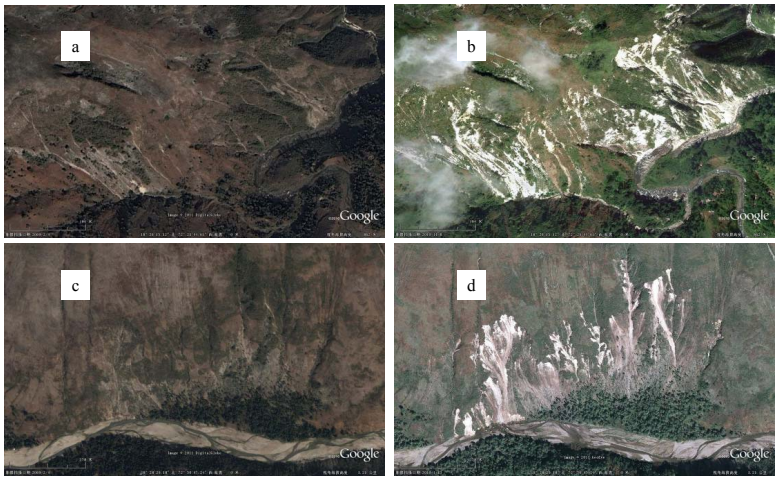

Fig. 7. Development of shallow disrupted landslides. The first site is located at 18°26′13.52″ N, 72°25′44.65″ W as shown in **(a)** and **(b)**. The dates of the images were 4 February 2009 and 8 November 2010, respectively. The second site (shown in **c** and **d**) is located at 18°28′29.18″ N, 72°30′47.24″ W. They were taken on 4 February 2009 and 13 January 2010, respectively. Upwards of all of the four images are north.

Fig. 8. (a) and **(b)** are two rock falls occurred at (18°28′07.75″ N, 72°29′15.00″ W) and (18°26′31.30″ N, 72°49′44.20″ W), respectively. **(a)** was taken on 13 January 2010 (upward is northeast) and **(b)** was taken on 25 January 2010 (upward is south). **(c)** is located at 18°28′51.78″ N, 72°26′42.00″ W, taken on 13 January 2010 and upward is north. **(d)** shows several rock falls at 18°19′38.90″ N, 72°40′01.32″ W, and the images was taken on 25 January 2010 (upward is west).

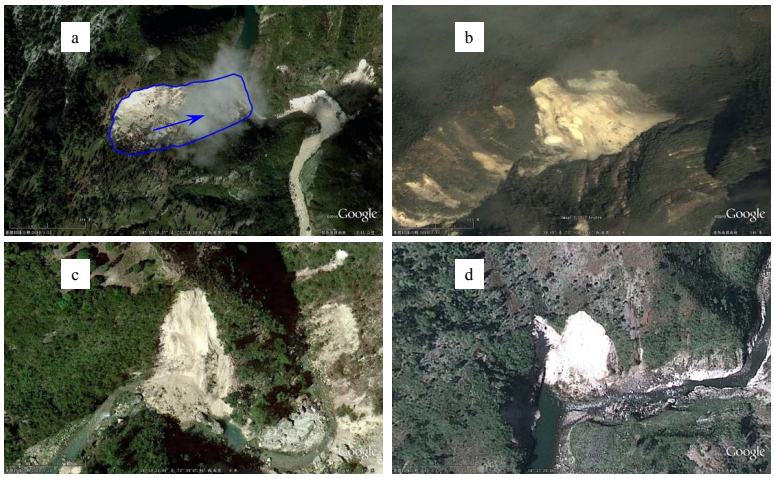

Fig. 9. Several rock slides triggered by the Haiti earthquake. **(a)** shows a rock slide located at 18°17′50.27″ N, 72°38′38.01″ W. The image was taken on 25 January 2010 (upward is west). **(b)** is located at 18°21′38.49″ N, 72°42′14.65″ W. The image was taken on 14 January 2010 (upward is north). **(c)** is located at 18°19′25.09″ N, 72°39′07.99″ W. The image was taken on 25 January 2010 (upward is west). **(d)** is located at 18°27′20.60″ N, 72°24′19.85″ W, and the image was taken on 13 January 2010 (upward is west).

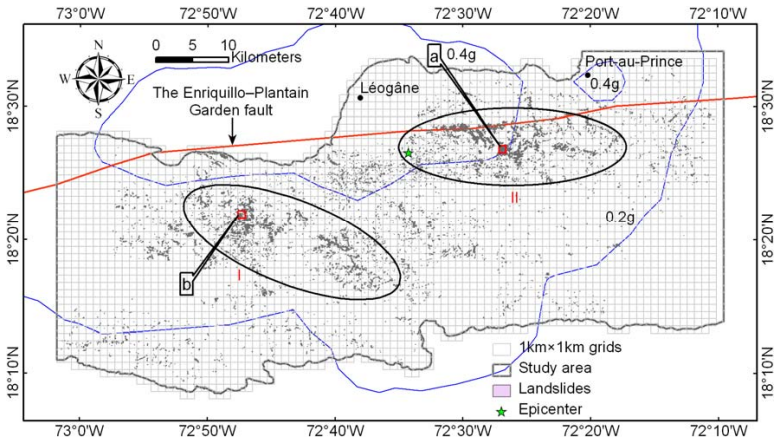

Fig. 10. Spatial distribution of landslides triggered by the Haiti earthquake. Blue lines represent PGA contours downloaded from US Geological Survey (2010). I and II are two landslide high density areas. We also constructed 1 km × 1 km grid cells (shown in grey). The red square a represents the grid cell with the highest value of landslide number density and landslide area percentage, and b represents the grid cell with the highest value of landslide erosion thickness.

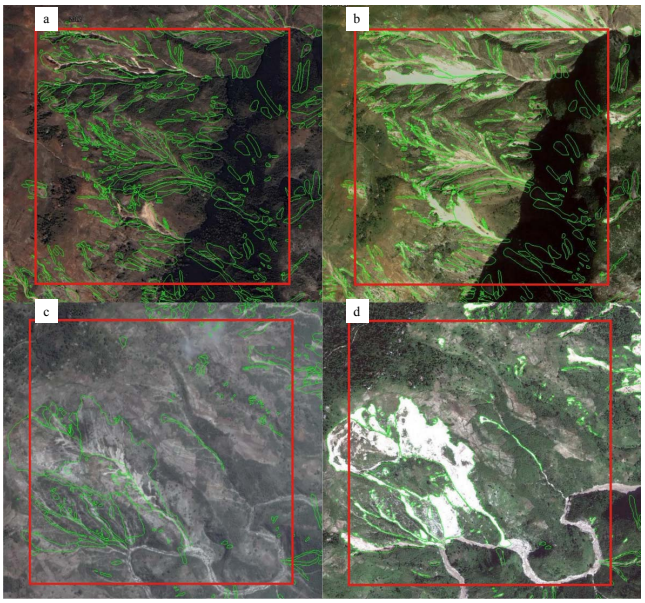

Fig. 11. Examples of 1 km × 1 km grids pre- and post-earthquake images. **(a)** taken on 4 February 2009, **(b)** taken on 21 January 2010, **(c)** taken on 2 June 2005, and **(d)** taken on 23 October 2010. The red square in **(a)** and **(b)** show the grid of the largest landslide number density and landslide area percentage located at the grid a in the Fig. 10, and the red square in **(c)** and **(d)** show the grid of the largest landslide erosion thickness located at the grid b in the Fig. 10.

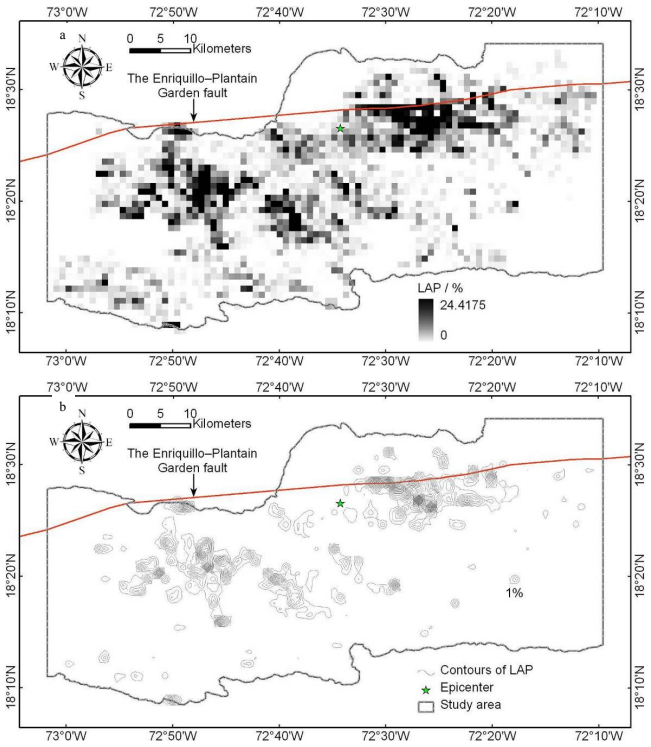

Fig. 12. Distribution maps of landslide area percentage of the study area. **(a)** Grid map, **(b)** contour map.

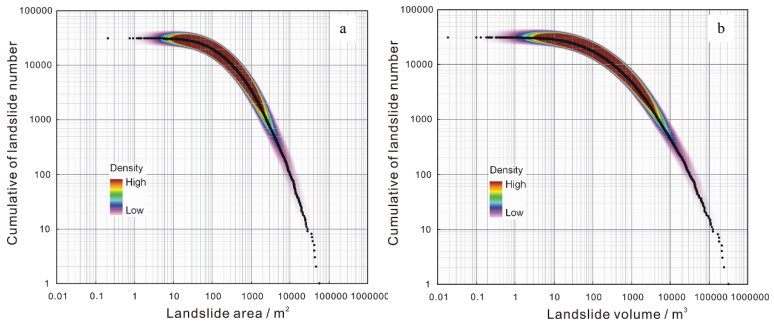

Fig. 13. Correlations between cumulative landslide number and landslide scale. **(a)** Landslide area, **(b)** landslide volume.

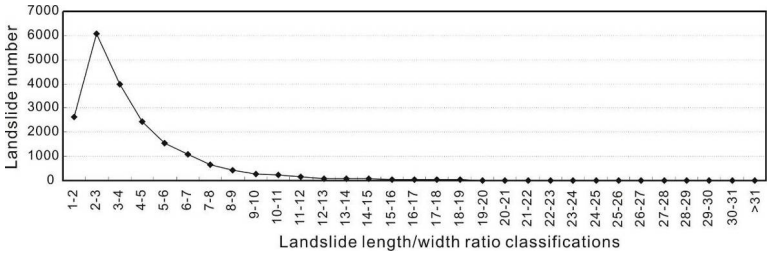

Fig. 14. Landslide length/width ratio distribution.

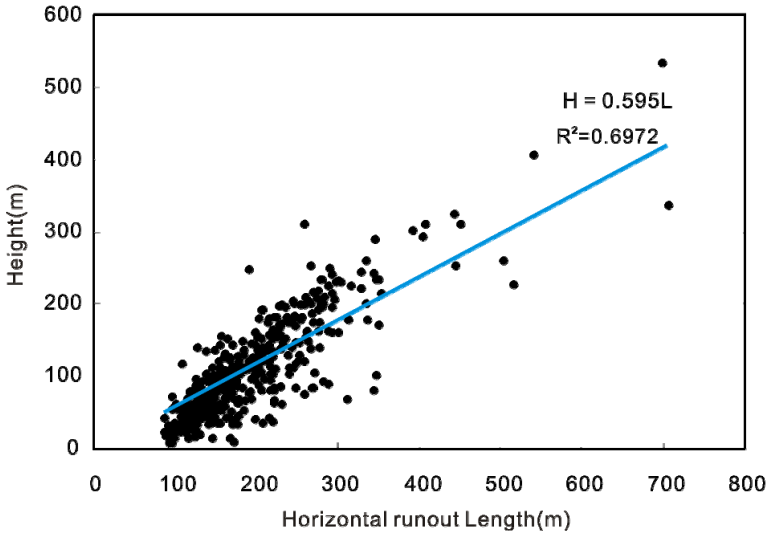

Fig. 15. Relationship between landslide height and horizontal runout length. A total of 453 landslides of area larger than 10 000 m^2 triggered by the Haiti earthquake were used to carry out the statistics.

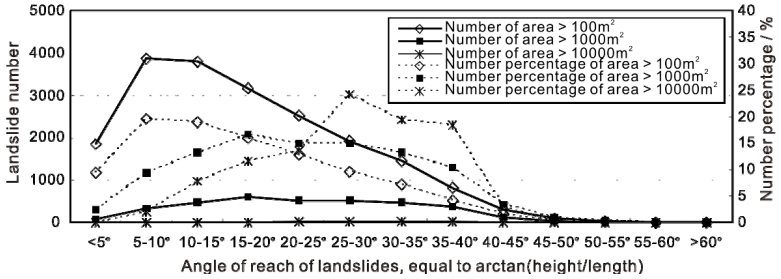

Fig. 16. Landslide angle of reach [arctan(height/length)] distribution.

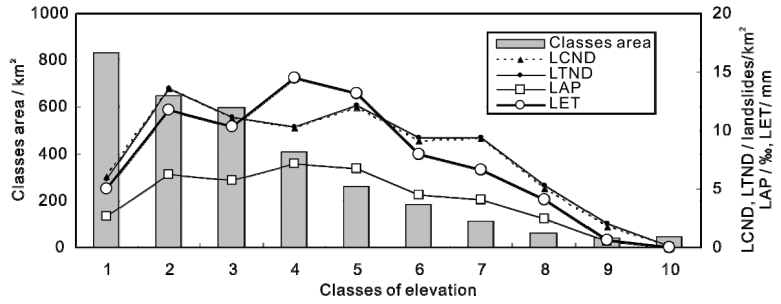

Fig. 17. Relationship of co-seismic landslide abundances with elevation. 1: 0–200 m, 2: 200–400 m, 3: 400–600 m, 4: 600–800 m, 5: 800–1000 m, 6: 1000–1200 m 7: 1200–1400 m, 8: 1400–1600 m 9: 1600–1800 m, 10: 1800–2275.88 m.

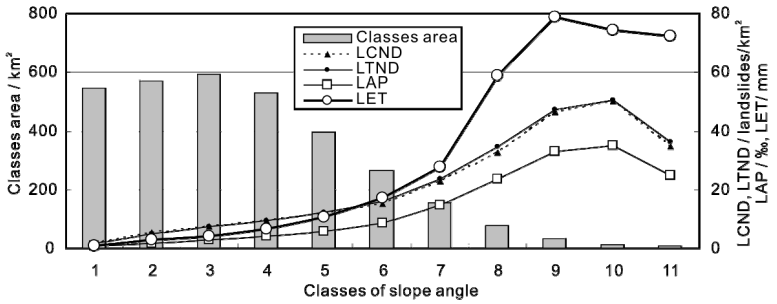

Fig. 18. Relationships of co-seismic landslide abundances with slope angles. 1: 0–5°, 2: 5–10°, 3: 10–15°, 4: 15–20°, 5: 20–25°, 6: 25–30°, 7: 30–35°, 8: 35–40°, 9: 40–45°, 10: 45–50°, 11: 50–75.83°.

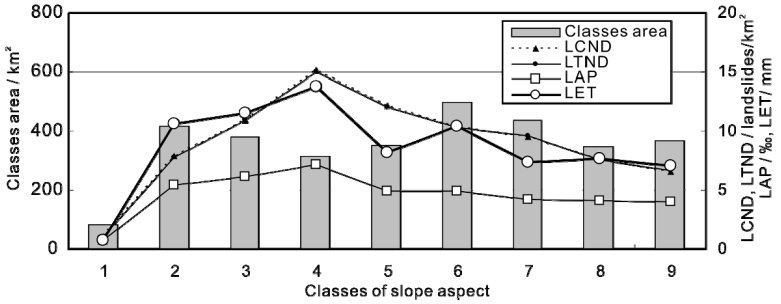

Fig. 19. Relationships of co-seismic landslide abundance with slope aspect. 1: Flat, 2: north, 3: northeast, 4: east, 5: southeast 6: south, 7: southwest, 8: west, and 9: northwest.

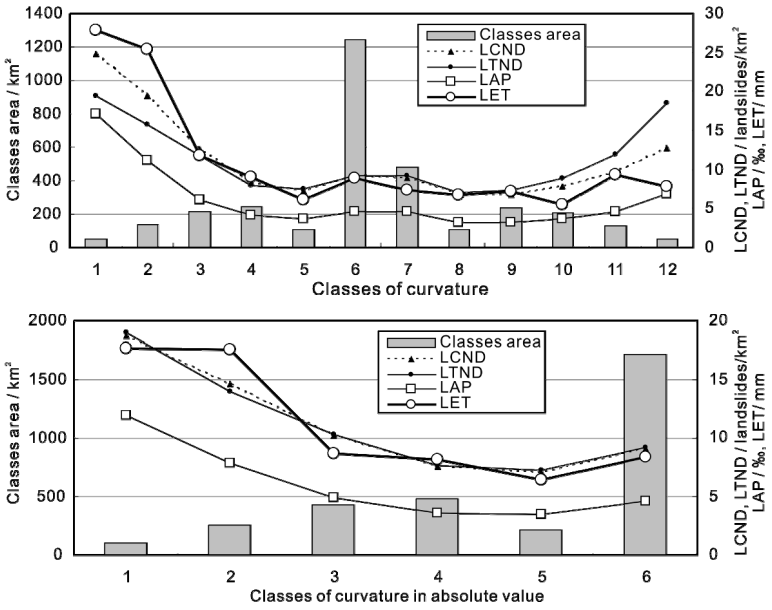

Fig. 20. Relationships between co-seismic landslides and slope curvature. **(a)** Classes divided considering the sign of slope curvature: 1: < −2, 2: −2 to −1, 3: −1 to −0.5, 4: −0.5 to −0.2, 5: −0.2 to −0.1, 6: −0.1 to 0, 7: 0–0.1, 8: 0.1–0.2, 9: 0.2–0.5, 10: 0.5–1, 11: 1–2, and 12: > 2. **(b)** Classes divided without considering the sign of slope curvature: 1: < −2 and > 2, 2: −2 to −1 and 1–2, 3: −1 to −0.5 and 0.5–1, 4: −0.5 to −0.2 and 0.2–0.5, 5: −0.2 to −0.1 and 0.1–0.2, 6: −0.1 to 0.1.

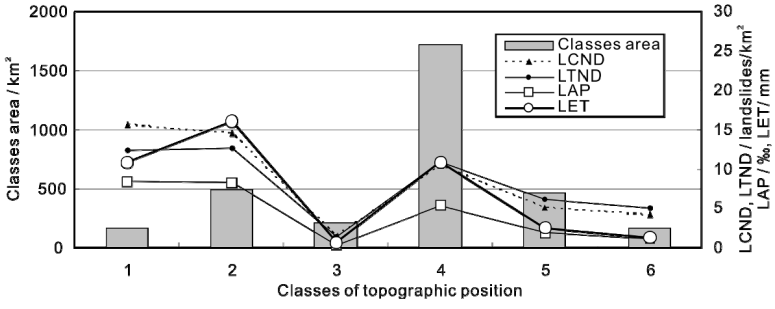

Fig. 21. Relationships between co-seismic landslides and topographic position. 1: Valleys, 2: lower slopes, 3: gentle slopes, 4: steep slopes, 5: upper slopes, and 6: ridges.

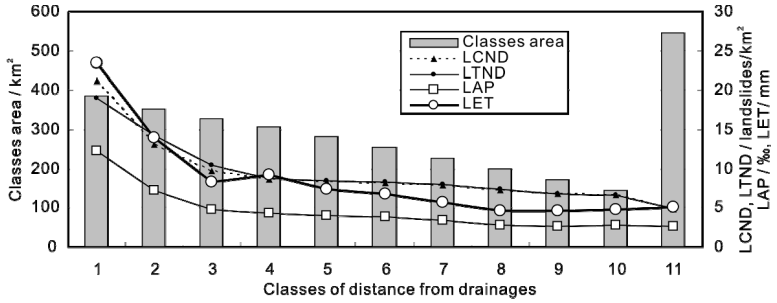

Fig. 22. Relationships of co-seismic landslides and distance from drainages. 1: 0–100 m, 2: 100–200 m, 3: 200–300 m, 4: 300–400 m, 5: 400–500 m, 6: 500–600 m, 7: 600–700 m, 8: 700–800 m, 9: 800–900 m, 10: 900–1000 m, and 11: > 1000 m.

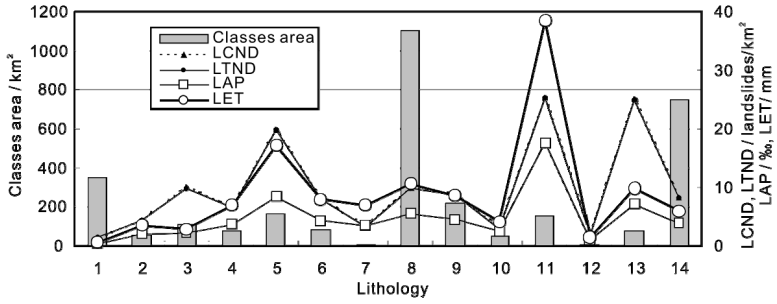

Fig. 23. Relationship of landslide proxies with lithology. 1: Qa, 2: Qc, 3: P, 4: Ms, 5: Mi, 6: O, 7: Es, 8: Ems, 9: Ep, 10: Pi, 11: Cs, 12: Cc, 13: Ca, and 14: Cb.

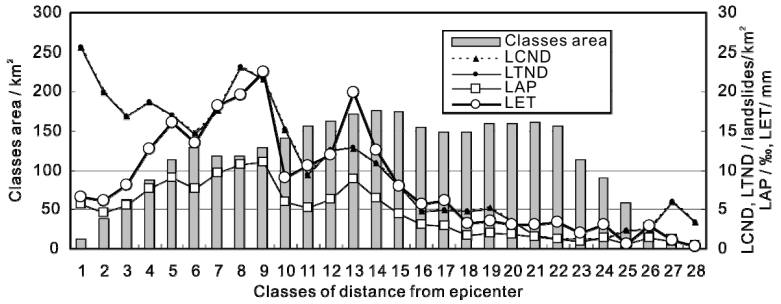

Fig. 24. Relationship of co-seismic landslides and distance from epicenter. 28 classes were divided according to 2 km intervals from the epicenter.

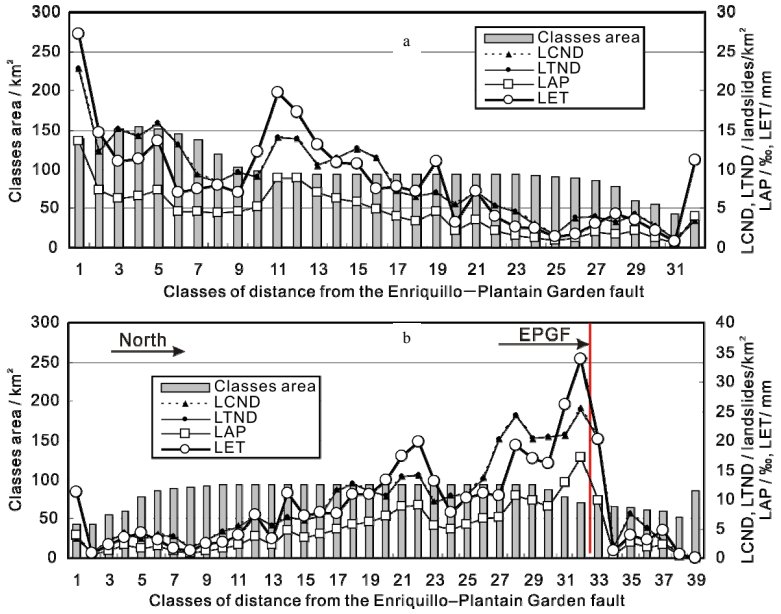

Fig. 25. Relationships of co-seismic landslides and distance from the Enriquillo–Plantain Garden fault. **(a)** Without considering the differences on the two sides of the fault, **(b)** considering the differences on the two sides of the fault.

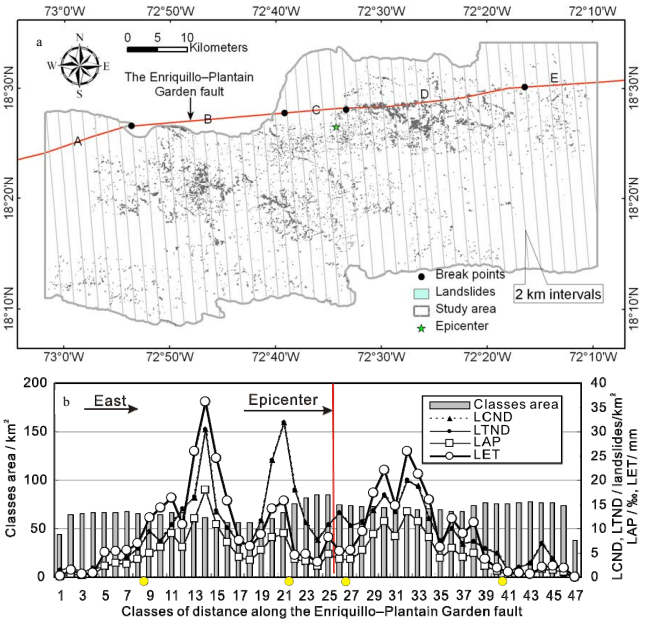

Fig. 26. (a) Segments of the Enriquillo–Plantain Garden fault and 2 km bands for classifying distance along the fault. A: Miragoane segment, B: Goave segment, C: Dufort segment, D: Momance segment, and E: Dumay segment. **(b)** Relation of co-seismic landslides and distance along the Enriquillo–Plantain Garden fault are also presented. 47 classes with 2 km intervals were analyzed, and the epicenter is located between classes 25 and 26. The yellow points represent the boundaries of the five segments of the Enriquillo–Plantain Garden fault.

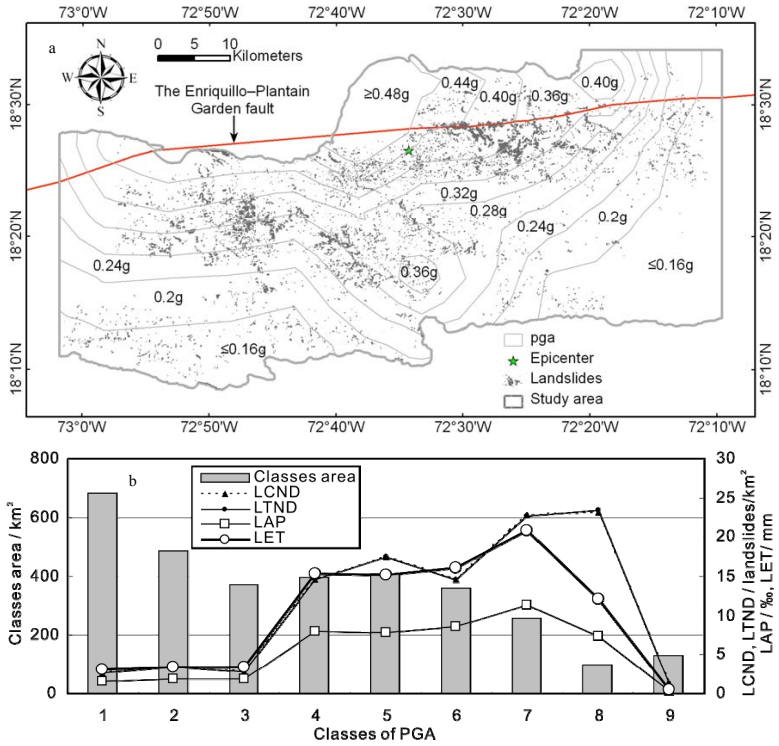

Fig. 27. (a) Distribution of PGA values of the study area and **(b)** relationships of co-seismic landslides and PGA. 1: ≤ 0.16 g, 2: 0.2 g, 3: 0.24 g, 4: 0.28 g, 5: 0.32 g, 6: 0.36 g, 7: 0.4 g, 8: 0.44 g, and 9: ≥ 0.48 g.

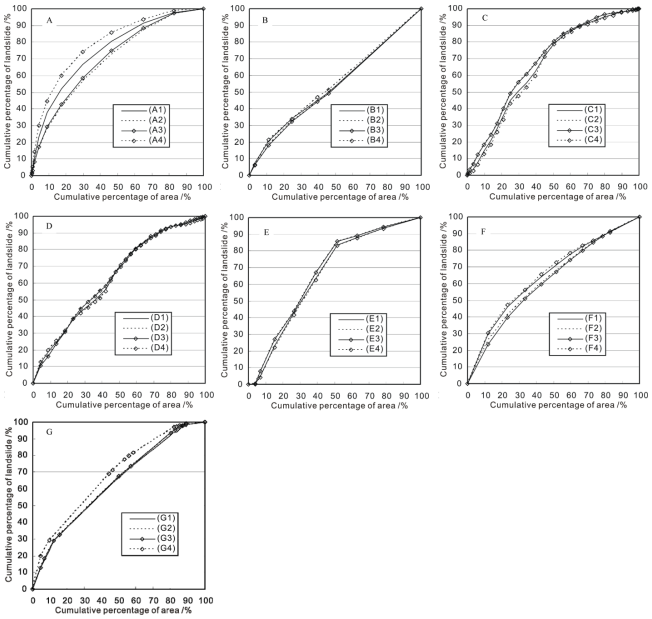

Fig. 28. Cumulative landslide area curves to analyze the influence of the 7 impact parameters on the landslide occurrences, separately shown by different impact parameters. **(A)** Slope angle, **(B)** slope curvature, **(C)** distance from epicenter, **(D)** distance from the Enriquillo–Plantain Garden fault, **(E)** PGA, **(F)** distance from drainages, and **(G)** lithology. The curves are: 1: landslide area, 2: landslide centroid point number, 3: landslide top point number, and 4: landslide accumulation material volume.

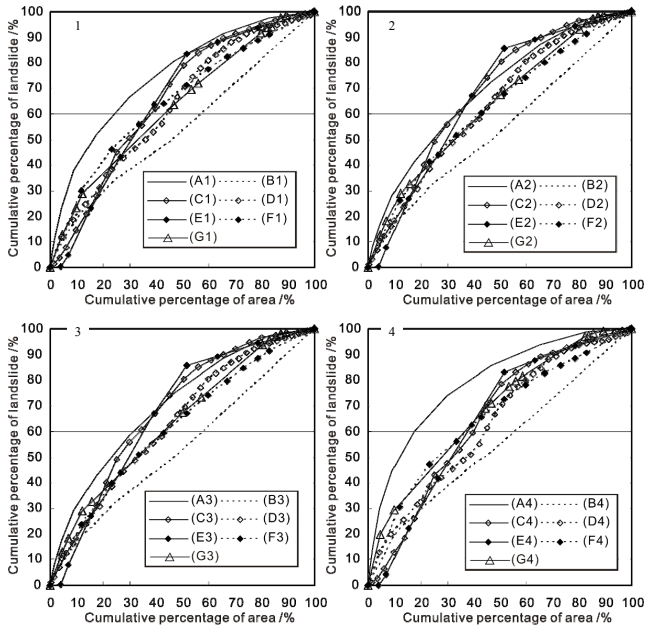

Fig. 29. Cumulative landslide area curves to analyze the influence of the 7 impact parameters on the landslide occurrences, separately shown by different landslide proxies. **(1)** Landslide area, **(2)** landslide centroid point number, **(3)** landslide top point number, and **(4)** landslide accumulation material volume. The curves are: A: slope angle, B: slope curvature, C: distance from epicenter, D: distance from the Enriquillo–Plantain Garden fault, E: PGA, and F: distance from drainages.

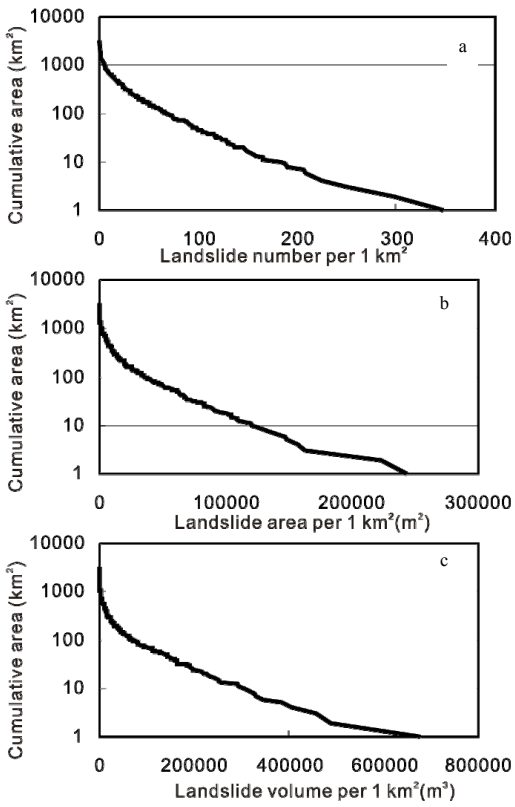

Fig. 30. Curves of LND, LAP, and LET with the area distribution. **(a)** LND (centroid); **(b)** LAP; **(c)** LET.